INTERNATIONAL JOURNAL FOR NUMERICAL METHODS IN ENGINEERING
Int. J. Numer. Meth. Engng 2006; **66**:1955–1989
Published online 13 January 2006 in Wiley InterScience (www.interscience.wiley.com). DOI: 10.1002/nme.1614

Efficient thermo-mechanical model for solidification processes

Seid Koric*, † and Brian G. Thomas‡

Mechanical and Industrial Engineering Department and National Center for Supercomputing Applications-NCSA, University of Illinois at Urbana-Champaign, 1206 W. Green Street, Urbana, IL 61801, U.S.A.

SUMMARY

A new, computationally efficient algorithm has been implemented to solve for thermal stresses, strains, and displacements in realistic solidification processes which involve highly nonlinear constitutive relations. A general form of the transient heat equation including latent-heat from phase transformations such as solidification and other temperature-dependent properties is solved numerically for the temperature field history. The resulting thermal stresses are solved by integrating the highly nonlinear thermo-elastic-viscoplastic constitutive equations using a two-level method. First, an estimate of the stress and inelastic strain is obtained at each local integration point by implicit integration followed by a bounded Newton–Raphson (NR) iteration of the constitutive law. Then, the global finite element equations describing the boundary value problem are solved using full NR iteration. The procedure has been implemented into the commercial package Abaqus (*Abaqus Standard Users Manuals*, v6.4, Abaqus Inc., 2004) using a user-defined subroutine (UMAT) to integrate the constitutive equations at the local level. Two special treatments for treating the liquid/mushy zone with a fixed grid approach are presented and compared. The model is validated both with a semi-analytical solution from Weiner and Boley (*J. Mech. Phys. Solids* 1963; **11**:145–154) as well as with an in-house finite element code CON2D (*Metal. Mater. Trans. B* 2004; **35B**(6):1151–1172; Continuous Casting Consortium Website. http://ccc.me.uiuc.edu [30 October 2005]; *Ph.D. Thesis*, University of Illinois, 1993; *Proceedings of the 76th Steelmaking Conference*, *ISS*, vol. 76, 1993) specialized in thermo-mechanical modelling of continuous casting. Both finite element codes are then applied to simulate temperature and stress development of a slice through the solidifying steel shell in a continuous casting mold under realistic operating conditions including a stress state of generalized plane strain and with actual temperature-dependent properties. Other local integration methods as well as the explicit initial strain method used in CON2D for solving this problem are also briefly reviewed and compared. Copyright © 2006 John Wiley & Sons, Ltd.

KEY WORDS: continuous casting; finite elements; Abaqus; UMAT; solidification

*Correspondence to: Seid Koric, Mechanical and Industrial Engineering Department & National Center for Supercomputing Applications-NCSA, University of Illinois at Urbana-Champaign, 1206 W. Green Street, Urbana, IL 61801, U.S.A.
†E-mail: skoric@ncsa.uiuc.edu
‡E-mail: bgthomas@uiuc.edu

Received 5 July 2005
Revised 4 November 2005
Accepted 10 November 2005

1. INTRODUCTION

Many manufacturing and fabrication processes such as foundry shape casting, continuous casting and welding, involve solidification phenomena. Accurate calculation of the distribution of temperature and stress during the early stages of solidification is important for correct prediction of surface shape and cracking problems in processes such as the continuous casting of steel. In 1963, Weiner and Boley [1] derived a semi-analytical solution for the thermal stresses arising during the solidification of a semi-infinite plate. Although that work oversimplifies the complex physical phenomena of solidification, it has become a useful benchmark problem for the verification of numerical models [2–6]. The constitutive models used in previous work to investigate thermal stresses during continuous casting first adopted simple elastic–plastic laws [1, 7, 8]. Later, separate creep laws were added [9, 10]. With the rapid advance of computer hardware, more computationally challenging elastic-viscoplastic models have been used [2, 3, 6, 11–18] which treat the phenomena of creep and plasticity together since only the combined effect is measurable. Most models use a Lagrangian approach with a fixed mesh due to its easy implementation, although an alternative Eularian–Langrangian approach has also been used [6, 14]. Schemes to integrate the viscoplastic laws range from easy-to-implement explicit methods [11, 12], to robust but complex implicitly based algorithms [2, 3], generally using in-house codes.

It is a considerable challenge to implement the unified approach of these previous in-house models into a fully three-dimensional (3D) analysis, and including other important phenomena such as contact. Such analysis would enable correct reproduction of the true 3D mechanical state in casting processes with complex geometry or with complex loading conditions. On the other hand, the easy-to-use commercial finite-element packages are now fully capable of handling 3D problems, having rich element libraries, fully imbedded pre- and post-processing capabilities, advanced modelling features such as contact algorithms, and can take full advantage of parallel-computing capabilities. Unfortunately, these commercial packages have given little effort to provide integration schemes that are robust enough to handle the highly nonlinear elastic-viscoplastic laws arising during casting, so are consequently very slow and prone to convergence problems.

This work implements and compares robust local viscoplastic integration schemes from an in-house code CON2D into the commercial finite element package Abaqus via its user-defined material subroutine UMAT.

In Section 2, the thermal governing equations and their finite-element implementations into Abaqus and CON2D are introduced. Section 3 presents the mechanical governing equations and the thermo-viscoplastic constitutive models. In Section 4, the global solution of this boundary value problem is described with two different materially nonlinear solution strategies using Abaqus and CON2D. Sections 5 and 7 provide detailed information on the local integration schemes and their coding. Two special treatments for liquid/mushy zone are introduced in Section 6. The new model is validated against semi-analytical solution and CON2D in Section 9. Finally in Section 10, a real-world simulation of a typical continuous casting process is performed with both codes using realistic temperature-dependent properties. The results are compared and CPU times are benchmarked. In order to focus on the improvements achieved in this work regarding the numerical treatment of the constitutive equations, other important phenomena such as contact between the mold and strand with gap-dependent interface conductivity, and ferrostatic pressure, are avoided in this paper, even though they have been fully

implemented into both codes. This work aims to open the door for realistic 3D computational modelling of complex solidification processes, by substantially improving the efficiency of commercial software available to the wider academic and industrial research communities.

1.1. Notation

Both standard tensor and indicial notations are used throughout this work. Here is a list of some of important notations and symbols.

	Tensor notation	Indicial notation
Fourth-order tensors	$\underline{\underline{\mathbf{D}}}$	D_{ijkl}
Second-order tensors	$\boldsymbol{\sigma}, \boldsymbol{\sigma}', \boldsymbol{\varepsilon}$	$\sigma_{ij}, \sigma'_{ij}, \varepsilon_{ij}$
Vectors	$\mathbf{u}, \mathbf{b}$	u_i, b_i
Scalars	T, μ, κ	T, μ, κ
Vector gradient	$\nabla \mathbf{u}$	$u_{i,j}$
Scalar gradient	∇T	$T_{,i}$
Divergence of tensor	$\nabla \cdot \boldsymbol{\sigma}$	$\sigma_{ij,j}$
Identity second-or. tensor	$\mathbf{I}$	δ_{ij}
Identity fourth-or. tensor	$\underline{\underline{\mathbf{I}}}$	$\delta_{ik}\delta_{jl}$
Inner tensor product	$\underline{\underline{\mathbf{D}}} : \boldsymbol{\varepsilon}$	$D_{ijkl}\varepsilon_{kl}$
Outer tensor product	$\mathbf{I} \otimes \mathbf{I}$	$\delta_{ij}\delta_{kl}$

δ_{ij} is Kronecker's delta defined by

$$\delta_{ij} = \begin{cases} 1 & \text{if } i = j \\ 0 & \text{if } i \neq j \end{cases}$$

Symmetric second-order tensors are often written as column vectors '{}', while symmetric fourth-order tensors are written as square matrices '[ ]'—following the Voigt notation [10].

$$\{\sigma\} = \{\sigma_x, \sigma_y, \sigma_x, \sigma_{xy}, \sigma_{xz}, \sigma_{yz}\}^{\mathrm{T}}, \quad \{\varepsilon\} = \{\varepsilon_x, \varepsilon_y, \varepsilon_z, \varepsilon_{xy}, \varepsilon_{xz}, \varepsilon_{yz}\}^{\mathrm{T}}$$

2. THERMAL GOVERNING EQUATIONS AND THEIR FINITE ELEMENT IMPLEMENTATIONS

The local form of the transient energy equation is given in Equation (1a) [11]

$$\rho\left(\frac{\partial H(T)}{\partial t}\right) = \nabla \cdot (k(T)\nabla T) \tag{1a}$$

along with boundary conditions:
Prescribed temperature on A_T

$$T = \hat{T}(\mathbf{x}, t)$$

Prescribed surface flux on A_q

$$(-k\nabla T) \cdot \mathbf{n} = \hat{q}(\mathbf{x}, t) \tag{1b}$$

Surface convection on A_h

$$(-k\nabla T)\cdot\mathbf{n}=h(T-T_\infty)$$

where ρ is density, k the isotropic temperature-dependent conductivity, H the temperature-dependent enthalpy, which includes the latent heat of solidification. $\hat{T}$ is a fixed temperature at the boundary A_T, $\hat{q}$ is the prescribed heat flux at the boundary A_q, h the film convection coefficient prescribed at the boundary A_h, where T_∞ is the ambient temperature, and $\mathbf{n}$ is the unit normal vector of the surface of the domain.

The commercial finite-element package Abaqus uses the backward-difference algorithm for time integration [19]

$$\dot{H}^{t+\Delta t}=\frac{H^{t+\Delta t}-H^t}{\Delta t} \tag{2}$$

After applying the standard Galerkin finite-element method to Equation (1a) [19], the weak form is established in Equation (3) using the common notation for element shape functions and their spatial derivatives $[N]$ and $[B]$, respectively.

$$\int_V [N]^{\mathrm{T}}\dot{H}\,\mathrm{d}V+\int_V [N]^{\mathrm{T}}k(t)\frac{\partial T}{\partial\mathbf{x}}\,\mathrm{d}V=\int_{A_q}[N]^{\mathrm{T}}\hat{q}\,\mathrm{d}A+\int_{A_h}[N]^{\mathrm{T}}h(T-T_0)\,\mathrm{d}A \tag{3}$$

Using Equation (2) for time discretization of (3), the following nonlinear system is established

$$\frac{1}{\Delta t}\int_V [N]^{\mathrm{T}}\rho(H^{t+\Delta t}-H^t)\,\mathrm{d}V+\int_V\frac{\partial[N]^{\mathrm{T}}}{\partial\mathbf{x}}k(T)\frac{\partial T}{\partial\mathbf{x}}\,\mathrm{d}V$$
$$-\int_{A_q}[N]^{\mathrm{T}}\hat{q}\,\mathrm{d}A-\int_{A_h}[N]^{\mathrm{T}}h(T-T_0)\,\mathrm{d}A=0 \tag{4}$$

Abaqus solves the nonlinear system, Equation (4), incrementally, i.e. achieving equilibrium balance at every time increment Δt by utilizing the modified Newton–Raphson (NR) iteration scheme given in (5) for each iteration i.

$$\left[\frac{1}{\Delta t}\int_V [N]^{\mathrm{T}}\rho\left(\frac{\mathrm{d}H}{\mathrm{d}T}\right)_i^{t+\Delta t}[N]\,\mathrm{d}V+\int_V[B]^{\mathrm{T}}k_i^{t+\Delta t}[B]\,\mathrm{d}V-\int_{A_h}[N]^{\mathrm{T}}h[N]\,\mathrm{d}A\right]\{\Delta T_i^{t+\Delta t}\}$$
$$=\int_{A_q}[N]^{\mathrm{T}}\hat{q}\,\mathrm{d}A+\int_{A_h}[N]^{\mathrm{T}}h(T_i^{t+\Delta t}-T_0)\,\mathrm{d}A-\frac{1}{\Delta t}\int_V[N]^{\mathrm{T}}\rho(H_i^{t+\Delta t}-H^t)\,\mathrm{d}V$$
$$-\int_V\frac{\partial[N]^{\mathrm{T}}}{\partial\mathbf{x}}k^t\left(\frac{\partial T^t}{\partial\mathbf{x}}\right)\mathrm{d}V \tag{5}$$

Equation (5) is solved for $\{\Delta T_i^{t+\Delta t}\}$ and then used to update the temperature solution, Equation (6) until convergence is achieved at every point in the domain at time $t+\Delta t$.

$$\{T_{i+1}^{t+\Delta t}\}=\{T_i^{t+\Delta t}\}+\{\Delta T_{i+1}^{t+\Delta t}\} \tag{6}$$

The term $(\mathrm{d}H/\mathrm{d}T)^{t+\Delta t}$ is an effective specific heat which is greatly enlarged over the phase-change temperature interval $T_{\mathrm{sol}} < T^{t+\Delta t} < T_{\mathrm{liq}}$ owing to the evolution of latent heat H_f. Here T_{sol} and T_{liq} are the solidus and liquidus temperatures, respectively. The temperature solution (history) for each material point is stored in a result file that is used in the subsequent mechanical analysis.

CON2D solves Equation (3) explicitly using the special averaging technique suggested by Lemmon [20] to evaluate the effective specific heat, as given in Equation (7)

$$\frac{\mathrm{d}H}{\mathrm{d}T} = \sqrt{\frac{(\partial H/\partial x)^2 + (\partial H/\partial y)^2}{(\partial T/\partial x)^2 + (\partial T/\partial y)^2}} \tag{7}$$

A three-level time-stepping method proposed by Dupont *et al.* [21] was adopted for CON2D to explicitly solve Equation (3). Assuming the current time is $t + \Delta t$, the previous two time steps are t, and $t - \Delta t$, respectively. The temperature vector $\{T\}$ and its time derivative vector $\{\dot{T}\}$ are given as

$$\{T\} = \tfrac{1}{4}\{3T^{t+\Delta t} + T^{t-\Delta t}\} \tag{8}$$

$$\{\dot{T}\} = \left\{\frac{T^{t+\Delta t} - T^{t}}{\Delta t}\right\} \tag{9}$$

After some rearranging this leads to an explicit matrix equation to be solved for temperature at the current time:

$$\left[\frac{3}{4}[K] + \frac{[C]}{\Delta t}\right]\{T^{t+\Delta t}\} = \{F_q\} - \frac{1}{4}[K]\{T^{t-\Delta t}\} + \frac{[C]}{\Delta t}\{T^{t}\} \tag{10a}$$

where $[K]$ is the conductance (tangent) matrix, $[C]$ the capacitance matrix, and $\{F_q\}$ the heat flow load vector are defined as

$$[C] = \int_V [N]^{\mathrm{T}} \rho \left(\frac{\mathrm{d}H}{\mathrm{d}T}\right)^{t+\Delta t} [N]\,\mathrm{d}V, \quad [K] = \int_V [B]^{\mathrm{T}} k^t [B]\,\mathrm{d}V, \quad \{F_q\} = \int_{A_q} [N]^{\mathrm{T}} \hat{q}\,\mathrm{d}A \tag{10b}$$

CON2D incrementally solves Equation (10a) for $\{T^{t+\Delta t}\}$. It couples the transient heat transfer and stress analysis; within each time increment, temperature is solved first and then subsequently used for the stress distribution. This procedure is repeated for every increment.

3. MECHANICAL GOVERNING EQUATIONS

Solidification involves small strain, so the assumption of small strain is adopted in this work. The thermal strains which dominate thermo-mechanical behaviour during solidification are in the order of only a few percent, or cracks will form [22]. Several previous solidification models [2–6] confirm that the solidified metal part indeed undergoes only small deformation during initial solidification in the mold. The displacement spatial gradient $\nabla\mathbf{u} = \partial\mathbf{u}/\partial\mathbf{x}$ is small, so $\nabla\mathbf{u} : \nabla\mathbf{u} \approx 1$ and the linearized strain tensor is thus [23]:

$$\boldsymbol{\varepsilon} = \tfrac{1}{2}[\nabla\mathbf{u} + (\nabla\mathbf{u})^{\mathrm{T}}] \tag{11}$$

Then, the small strain formulation can be used, where Cauchy stress tensor is identified with the nominal stress tensor $\boldsymbol{\sigma}$, and $\mathbf{b}$ is the body force density with respect to initial configuration.

$$\nabla \cdot \boldsymbol{\sigma}(\mathbf{x}) + \mathbf{b} = 0 \tag{12a}$$

The boundary conditions are

$$\begin{aligned} \mathbf{u} &= \hat{\mathbf{u}} \quad \text{on } A_u \\ \boldsymbol{\sigma} \cdot \mathbf{n} &= \boldsymbol{\Phi} \quad \text{on } A_\Phi \end{aligned} \tag{12b}$$

where prescribed displacements $\hat{\mathbf{u}}$ on boundary surface portion A_u, and boundary surface tractions $\boldsymbol{\Phi}$ on portion A_Φ define a quasi-static boundary value problem. The rate representation of total strain in this elastic-viscoplastic model is given by

$$\dot{\boldsymbol{\varepsilon}} = \dot{\boldsymbol{\varepsilon}}_{\text{el}} + \dot{\boldsymbol{\varepsilon}}_{\text{ie}} + \dot{\boldsymbol{\varepsilon}}_{\text{th}} \tag{13}$$

where $\dot{\boldsymbol{\varepsilon}}_{\text{el}}$, $\dot{\boldsymbol{\varepsilon}}_{\text{ie}}$, $\dot{\boldsymbol{\varepsilon}}_{\text{th}}$ are the elastic, inelastic (plastic + creep), and thermal strain rate tensors, respectively. Stress rate $\dot{\boldsymbol{\sigma}}$ depends on elastic strain rate and in this case of linear isotropic material and negligible large rotations it is given by (14)

$$\dot{\boldsymbol{\sigma}} = \underline{\underline{\mathbf{D}}} : (\dot{\boldsymbol{\varepsilon}} - \dot{\boldsymbol{\varepsilon}}_{\text{ie}} - \dot{\boldsymbol{\varepsilon}}_{\text{th}}) \tag{14}$$

$\underline{\underline{\mathbf{D}}}$ is the fourth-order isotropic elasticity tensor given by (10a)

$$\underline{\underline{\mathbf{D}}} = 2\mu \underline{\underline{\mathbf{I}}} + (k_{\text{B}} - \tfrac{2}{3}\mu)\mathbf{I} \otimes \mathbf{I} \tag{15}$$

Here μ, k_{B} are the shear modulus and bulk modulus, respectively, and are in general functions of temperature, while $\underline{\underline{\mathbf{I}}}$, $\mathbf{I}$ are fourth- and second-order identity tensors.

3.1. Inelastic strain

Inelastic strain includes both strain-rate-independent plasticity and time-dependent creep. Creep is significant at the high temperatures of the solidification processes and is indistinguishable from plastic strain [2]. The inelastic strain-rate is defined here with a unified formulation using a single internal variable [24, 25], equivalent inelastic strain $\bar{\varepsilon}_{\text{ie}}$ to characterize the microstructure. For steel solidification considered here, the equivalent inelastic strain-rate $\dot{\bar{\varepsilon}}_{\text{ie}}$ is a function of equivalent stress $\bar{\sigma}$, temperature T, equivalent inelastic strain $\bar{\varepsilon}_{\text{ie}}$, and steel grade defined by its carbon content (%C).

$$\dot{\bar{\varepsilon}}_{\text{ie}} = f(\bar{\sigma}, T, \bar{\varepsilon}_{\text{ie}}, \%\text{C}) \tag{16}$$

$$\bar{\sigma} = \sqrt{\tfrac{3}{2}\sigma'_{ij}\sigma'_{ij}} \tag{17}$$

$\boldsymbol{\sigma}'$ is a deviatoric stress tensor defined by

$$\sigma'_{ij} = \sigma_{ij} - \tfrac{1}{3}\sigma_{kk}\delta_{ij} \tag{18}$$

The mild carbon steels treated in this work are assumed to harden isotropically, so the von Mises loading surface, associated plasticity, and normality hypothesis in the Prandtl–Reuss flow

law is applied [26, 27]:

$$(\dot{\varepsilon}_{\mathrm{ie}})_{ij} = \frac{3}{2}\frac{\dot{\bar{\varepsilon}}_{\mathrm{ie}}}{\bar{\sigma}}\sigma'_{ij} \tag{19}$$

$\dot{\bar{\varepsilon}}_{\mathrm{ie}}$ has a sign determined by the direction of the maximum principle inelastic strain, as defined in Equation (20) in order to achieve kinematic behaviour (Bauschinger effect) during reverse loading [2].

$$\dot{\bar{\varepsilon}}_{\mathrm{ie}} = c_S\sqrt{\tfrac{2}{3}(\dot{\varepsilon}_{\mathrm{ie}})_{ij}(\dot{\varepsilon}_{\mathrm{ie}})_{ij}} \quad \text{where } c_S = \begin{cases} \dfrac{\varepsilon_{\max}}{|\varepsilon_{\min}|}, & \varepsilon_{\max} \geqslant \varepsilon_{\min} \\ \dfrac{\varepsilon_{\min}}{|\varepsilon_{\max}|}, & \varepsilon_{\max} < \varepsilon_{\min} \end{cases} \tag{20}$$

3.2. Thermal strain

Thermal strains arise due to volume changes caused by both temperature differences and phase transformations, including solidification and solid-state phase changes between crystal structures, such as austenite and ferrite.

$$(\varepsilon_{\mathrm{th}})_{ij} = \int_{T_0}^{T} \alpha(T)\,\mathrm{d}T\,\delta_{ij} \tag{21}$$

where α is temperature-dependent coefficient of thermal expansion, and T_0 is the reference temperature. Thermal strain tensors in this work are calculated from the thermal linear expansion function, TLE [2, 3], which will be discussed later.

4. GLOBAL SOLUTION OF BOUNDARY VALUE PROBLEM, MATERIALLY NONLINEAR SOLUTION STRATEGIES IN ABAQUS AND CON2D

After applying the standard Galerkin finite element method to the materially nonlinear boundary value problem in Equation (12a), residual force $\{R\}$ is found, representing the imbalance between internal stress in the body and externally applied loads from body forces and surface tractions [28–30].

$$\{R\} = \int_V [B]^{\mathrm{T}}\{\sigma\}\,\mathrm{d}V - \left(\int_V [N]^{\mathrm{T}}\{b\}\,\mathrm{d}V + \int_{A_\Phi} [N]^{\mathrm{T}}\{\Phi\}\,\mathrm{d}A\right) \tag{22}$$

Equilibrium is satisfied when the residual force vanishes (at least within prescribed tolerance). Similarly, to its solution of the heat transfer equation (4), Abaqus solves Equation (22) incrementally. Using the full NR method, Equation (23), several 'global equilibrium iterations' 'i' are needed to achieve equilibrium by the end of every time increment Δt.

$$[K_{i-1}^{t+\Delta t}]\{\Delta u_{i-1}^{t+\Delta t}\} = \{P^{t+\Delta t}\} - \{S_{i-1}^{t+\Delta t}\} \tag{23}$$

Equation (23) is solved for $\{\Delta u_{i-1}^{t+\Delta t}\}$ and then used to update the displacement solution, Equation (24), until convergence is achieved everywhere at time $t + \Delta t$.

$$\{u_t^{t+\Delta t}\} = \{u_{i-1}^{t+\Delta t}\} + \{\Delta u_{i-1}^{t+\Delta t}\} \tag{24}$$

External load vector $\{P^{t+\Delta t}\}$ at time $t+\Delta t$ is defined as

$$\{P^{t+\Delta t}\} = \int_V [N]^{\mathrm{T}} \{b^{t+\Delta t}\}\, \mathrm{d}V + \int_{A_\Phi} [N]^{\mathrm{T}} \{\Phi^{t+\Delta t}\}\, \mathrm{d}A \tag{25}$$

Internal force $\{S^{t+\Delta t}\}$ at time $t+\Delta t$ is defined as

$$\{S^{t+\Delta t}\} = \int_V [B]^{\mathrm{T}} \{\sigma^{t+\Delta t}\}\, \mathrm{d}V \tag{26}$$

The tangent stiffness Matrix $[K^{t+\Delta t}]$ is defined in Equation (28) from the consistent tangent operator, or 'Jacobian' $[J]$, defined in Equation (27), which must be consistent with the local integration method to provide quadratic convergence of Equation (23) [31, 32]. Again $[B]$ contains spatial derivatives of the element shape functions $[N]$, while $\Delta\hat{\boldsymbol{\varepsilon}}^{t+\Delta t}$ is a 'guessed' mechanical strain increment, based on the current best displacement increment.

$$\underline{\underline{\mathbf{J}}} = \frac{\partial \boldsymbol{\sigma}^{t+\Delta t}}{\partial \Delta\hat{\boldsymbol{\varepsilon}}^{t+\Delta t}} \tag{27}$$

$$[K^{t+\Delta t}] = \int_V [B^{\mathrm{T}}][J][B]\, \mathrm{d}V \tag{28}$$

As shown in Figure 1, if the tolerance for NR convergence criteria is exceeded, a new NR iteration starts that performs the following tasks:

- New guess for mechanical strain increments is calculated from the current displacement increments.
- UMAT subroutine is called at all material points to perform constitutive model integration (also called local integration, stress update algorithm, or solution to boundary value problem) and returns updated stress, and Jacobian.
- Element internal forces and element tangent matrices are calculated and assembled into the global assembly.
- New global displacement field is calculated from (23) and (24) and convergence criterion is checked again.
- Once the NR convergence criterion is satisfied everywhere, a new increment of loading history is applied, based on the heat transfer solution for the next time step, and the whole process is repeated until the end of the loading history, which is defined as a STEP in Abaqus.

CON2D uses an Operator Splitting Technique [2, 33] with fully explicit initial-strain procedure [29, 34] to solve Equation (22) by alternating between the local and global steps without global iterations or consistent tangent operators [2, 3]. First, local integration of the constitutive equations is used to guess the inelastic strain rate $\{\hat{\dot{\varepsilon}}_{\mathrm{ie}}\}^{t+\Delta t}$ and stress at each material point, assuming total strain rate stays constant over the time step. The inelastic strain rate is converted to an initial strain increment as follows [11, 29]:

$$\{\hat{\sigma}\}^{t+\Delta t} = \{\sigma\}^t + [D]^{t+\Delta t}(\{\Delta\varepsilon\}^{t+\Delta t} - \{\Delta\varepsilon_0\}^{t+\Delta t}) \tag{29}$$

$$\{\Delta\varepsilon_0\}^{t+\Delta t} = \{\Delta\varepsilon_{\mathrm{th}}\}^{t+\Delta t} + \{\hat{\dot{\varepsilon}}_{\mathrm{ie}}\}\Delta t \tag{30}$$

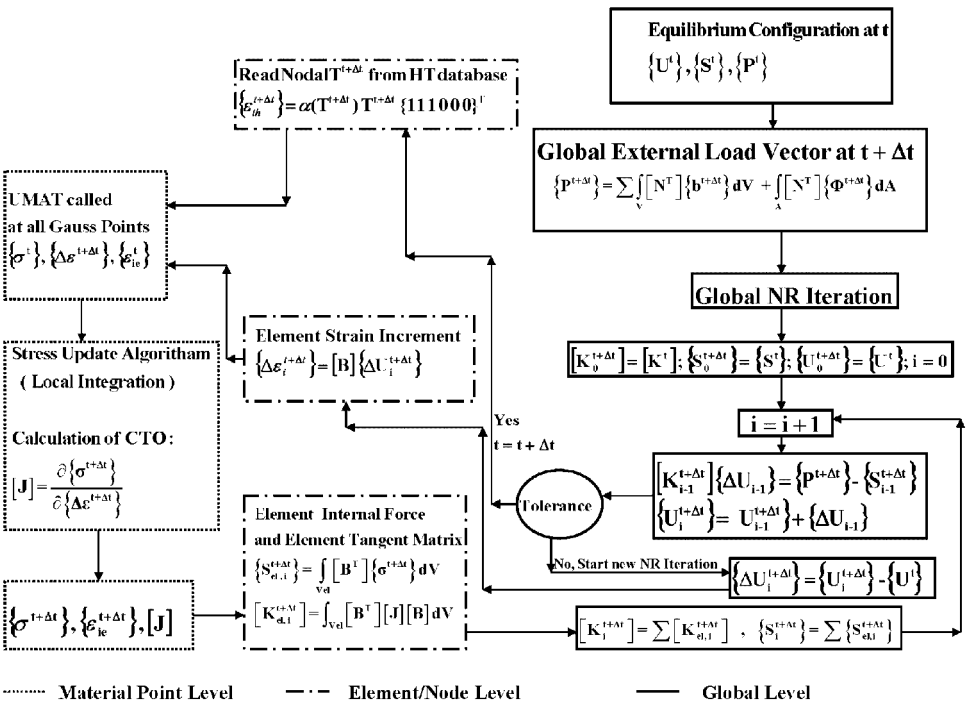

Figure 1. Flow chart for Abaqus solution of thermal mechanical problem, including local material-point level calculations in user-defined UMAT.

Then, the global equation (22) is manipulated into the following explicit system of linear equations given in Equation (31), which is solved for displacement increments only once for each time increment. The tangent matrix on the left-hand side of Equation (31) is the same as that of linear elasticity.

$$\sum \int_{V_{\mathrm{el}}} [B^{\mathrm{T}}][D][B]\,\mathrm{d}V\{\Delta d\}^{t+\Delta t} = \sum \int_{V_{\mathrm{el}}} [B^{\mathrm{T}}][D]\{\hat{\dot{\varepsilon}}_{\mathrm{ie}}\}^{t+\Delta t}\Delta t\,\mathrm{d}V + \sum \int_{V_{\mathrm{el}}} [B^{\mathrm{T}}][D] \times \{\Delta\varepsilon_{\mathrm{th}}\}^{t+\Delta t}\,\mathrm{d}V - \sum \int_{V_{\mathrm{el}}} [B^{\mathrm{T}}][D]\{\boldsymbol{\varepsilon}_{\mathrm{el}}\}^{t}\,\mathrm{d}V + \sum \int_{V_{\mathrm{el}}} [N^{\mathrm{T}}]\{b\}^{t+\Delta t}\,\mathrm{d}V + \sum \int_{A_\phi} [N^{\mathrm{T}}]\{\Phi\}^{t+\Delta t}\,\mathrm{d}A \quad (31)$$

Finally, the total values of displacement, inelastic strain and total strain are updated as follows:

$$\{d\}^{t+\Delta t} = \{d\}^{t} + \{\Delta d\}^{t+\Delta t}, \quad \{\Delta\varepsilon\}^{t+\Delta t} = [B]\{\Delta d\}^{t+\Delta t}, \quad \{\Delta\varepsilon_{\mathrm{ie}}\}^{t+\Delta t} = \{\hat{\dot{\varepsilon}}_{\mathrm{ie}}\}^{t+\Delta t}\Delta t \quad (32)$$

and stress is updated with Equation (33)

$$\{\sigma\}^{t+\Delta t} = \{\sigma\}^{t} + [D]^{t+\Delta t}(\{\Delta\varepsilon\}^{t+\Delta t} - \{\Delta\varepsilon_{\mathrm{ie}}\}^{t+\Delta t} - \{\Delta\varepsilon_{\mathrm{th}}\}^{t+\Delta t}) \quad (33)$$

Even though this simplified approach for solving the boundary value problem shows some small stress oscillations which are not found with the full global NR method from Abaqus, this method generally performs well with very low CPU cost.

5. LOCAL TIME INTEGRATION OF THE INELASTIC CONSTITUTIVE MODEL

Assuming that the total strain rate at time t is known from the previous time step, Equations (14), (16)–(20) constitute a nonlinear system with 15 unknowns (two tensors and three scalars) at every material point for a 3D problem. Owing to the highly strain-dependent inelastic responses, a robust integration scheme is required to solve this system over a generic time increment Δt. The solution obtained from this 'local' integration step from all material (gauss) points is used to update the global finite element equilibrium equation (22), and solved using the finite element procedure from Section 4.

Four different local integration methods are investigated in this work. Abaqus supports the CREEP subroutine where viscoplastic laws like (14) just need to be coded and Abaqus will integrate them with either its explicit, or implicit built-in algorithm followed by the full local NR scheme [28, 35]. Alternatively, implicit CREEP can work together with Abaqus built-in plasticity, which was used here as one approach to model the liquid/mushy zone.

On the other hand, an implicit integration technique based on Lush *et al.* [25], Zabaras and Arif [36] and later Zhu [3] in CON2D [2, 37] was used here to reduce the equation system to a pair of scalar equations with just two unknowns. These two equations are then solved with either a local bounded NR scheme or an explicit scheme from Nemat-Nasser and Li [38] and Nemat-Nasser and Chung [39]. Both these techniques are coded into Abaqus via its user-defined subroutine UMAT.

5.1. Implicit local integration (ODE) from CON2D

The system of ordinary differential equations defined at each material point are converted into two 'integrated' scalar equations and solved using either (1) bounded NR method; or (2) Nemat-Nasser method.

Knowing the state $(\boldsymbol{\sigma}^t, \boldsymbol{\varepsilon}_{\text{ie}}^t)$ at time t, the solution marches forward in time to determine the state at $t+\Delta t\,(\boldsymbol{\sigma}^{t+\Delta t}, \boldsymbol{\sigma}_{\text{ie}}^{t+\Delta t})$. The Euler backward method of integration is used to convert the system of ODEs at each material point, Equation (14), to the following equation system:

$$\sigma_{ij}^{t+\Delta t} = D_{ijkl}^{t+\Delta t}(\varepsilon_{kl}^t - (\varepsilon_{\text{th}}^t)_{kl} - (\varepsilon_{\text{ie}}^t)_{kl} + \Delta\varepsilon_{kl}^{t+\Delta t} - (\Delta\varepsilon_{\text{th}}^{t+\Delta t})_{kl} - (\Delta\varepsilon_{\text{ie}}^{t+\Delta t})_{kl}) \tag{34}$$

By using Equations (19) and (16), and by introducing $\Delta\hat{\varepsilon}_{kl}$, (which is the current best estimate of the total strain increment from the global solution of the nonlinear finite element equations), to replace $\Delta\varepsilon_{kl}^{t+\Delta t}$, Equation (34) becomes:

$$\sigma_{ij}^{t+\Delta t} = D_{ijkl}^{t+\Delta t}\left(\varepsilon_{kl}^t - (\varepsilon_{\text{th}}^t)_{kl} - (\varepsilon_{\text{ie}}^t)_{kl} + \Delta\hat{\varepsilon}_{kl} - (\Delta\varepsilon_{\text{th}}^{t+\Delta t})_{kl} - \frac{3}{2} f(T^{t+\Delta t}, \overline{\sigma}^{t+\Delta t}, \overline{\varepsilon}_{\text{ie}}^{t+\Delta t}, \%\text{C})\,\frac{\sigma_{kl}'^{\,t+\Delta t}}{\overline{\sigma}^{t+\Delta t}}\,\Delta t\right) \tag{35}$$

Similarly, the evolution of equivalent inelastic strain $\bar{\varepsilon}_{\text{ie}}$ equation (16) is integrated in (36)

$$\bar{\varepsilon}_{\text{ie}}^{t+\Delta t} = \bar{\varepsilon}_{\text{ie}}^{t} + f(T^{t+\Delta t}, \bar{\sigma}^{t+\Delta t}, \bar{\varepsilon}_{\text{ie}}^{t+\Delta t}, \%\text{C})\Delta t \tag{36}$$

Given the temperature solution from the Heat Transfer procedure, $\Delta\varepsilon_{\text{th}}^{t+\Delta t}$ is easy to find. Therefore, there are seven unknown scalars for 3D problems (six components of $\sigma_{ij}^{t+\Delta t}$ plus $\bar{\varepsilon}_{\text{ie}}^{t+\Delta t}$), and five for 2D problems. Solving nonlinear tensor equation (35) and nonlinear scalar equation (36) for these unknowns is computationally challenging.

Fortunately, Lush *et al.* [25] transformed the tensor equation (35) into a scalar equation for isotropic materials with isotropic hardening.

$$\bar{\sigma}^{t+\Delta t} = \bar{\sigma}^{*t+\Delta t} - 3\mu^{t+\Delta t} f(T^{t+\Delta t}, \bar{\sigma}^{t+\Delta t}, \bar{\varepsilon}_{\text{ie}}^{t+\Delta t}, \%\text{C})\Delta t \tag{37}$$

where $\bar{\sigma}^{*t+\Delta t}$ is equivalent stress of the trial stress tensor (elastic predictor) $\sigma_{ij}^{*t+\Delta t}$ defined in Equation (38)

$$\sigma_{ij}^{*t+\Delta t} = D_{ijkl}^{t+\Delta t}(\varepsilon_{kl}^{t} - (\varepsilon_{\text{th}}^{t})_{kl} - (\varepsilon_{\text{in}}^{t})_{kl} + \Delta\hat{\varepsilon}_{kl} - (\Delta\varepsilon_{\text{th}}^{t+\Delta t})_{kl}) \tag{38}$$

Equations (36) and (37) form a pair of highly nonlinear scalar equations to solve in the local step for the two unknowns $\bar{\varepsilon}_{\text{ie}}^{t+\Delta t}$ and $\bar{\sigma}^{t+\Delta t}$. Two solution methods that showed the best accuracy, convergence, and robustness in previous work [3] are implemented and tested.

5.1.1. Bounded NR solution of a pair of scalar equations. Lush *et al.* [25] and later Zhu [3] used a two-level iterative scheme to solve (36) and (37) that showed fast and robust convergence using different viscoplastic laws in Equation (16). Details of this scheme can be found in References [2, 3, 25], and here is a brief summary.

The main iterative loop, Level 1, solves Equation (36) for $\bar{\varepsilon}_{\text{ie}}^{t+\Delta t}$. Using this estimate for $\bar{\varepsilon}_{\text{ie}}^{t+\Delta t}$, Equation (37) is solved for $\bar{\sigma}^{t+\Delta t}$ using a bounded NR iteration scheme, which is called Level 2. The solution ($\bar{\sigma}^{t+\Delta t}$, $\bar{\varepsilon}_{\text{ie}}^{t+\Delta t}$) is substituted into Equation (36) and the estimate for $\bar{\varepsilon}_{\text{ie}}^{t+\Delta t}$ is corrected using a standard NR scheme on Level 1. The whole procedure is repeated until Equation (36) is satisfied within error tolerance.

Each Level 2 iteration i, upper and lower bounds are set on $\bar{\sigma}^{t+\Delta t}$. The initial lower bound is always zero. The first upper bound is that $\bar{\sigma}^{t+\Delta t}$ is positive.

$$\bar{\sigma}_{i}^{t+\Delta t} > 0 \quad \text{gives } \bar{\sigma}_{i}^{t+\Delta t} \leqslant \bar{\sigma}^{*t+\Delta t} \tag{39}$$

The second upper bound starts with the condition that f is positive:

$$f > 0 \quad \text{gives } f(\bar{\sigma}_{i}^{t+\Delta t}, \bar{\varepsilon}_{\text{ie}}^{t+\Delta t}) \leqslant \frac{\bar{\sigma}^{*t+\Delta t}}{3\mu\Delta t} \tag{40}$$

And also that f is invertible:

$$\bar{\sigma}^{t+\Delta t} = f^{-1}(\dot{\bar{\varepsilon}}_{\text{ie}}^{t+\Delta t}, \bar{\varepsilon}_{\text{ie}}^{t+\Delta t}) \tag{41}$$

By using (16), Equation (41) becomes:

$$\bar{\sigma}^{t+\Delta t} = f^{-1}(f(\bar{\sigma}_{i}^{t+\Delta t}, \bar{\varepsilon}_{\text{ie}}^{t+\Delta t}), \bar{\varepsilon}_{\text{ie}}^{t+\Delta t}) \tag{42}$$

Inserting (40) into (42) gives a second upper bound for $\overline{\sigma}_i^{t+\Delta t}$ assuming that f^{-1} is an incremental function with respect to $\dot{\overline{\varepsilon}}_{\text{ie}}^{t+\Delta t}$ and $\overline{\varepsilon}_{\text{ie}}^{t+\Delta t}$.

$$\overline{\sigma}_i^{t+\Delta t} \leqslant f^{-1}\left(\frac{\overline{\sigma}^{*t+\Delta t}}{3\mu\Delta t}, \overline{\varepsilon}_{\text{ie}}^{t+\Delta t}\right) \tag{43}$$

So, the bounds for $\overline{\sigma}_i^{t+\Delta t}$ are given in Equation (44)

$$\begin{aligned} \overline{\sigma}_{\text{lower}}^{t+\Delta t} &= 0 \\ \overline{\sigma}_{\text{upper}}^{t+\Delta t} &= \min\left(\overline{\sigma}^{*t+\Delta t}, f^{-1}\left(\frac{\overline{\sigma}^{*t+\Delta t}}{3\mu\Delta t}, \overline{\varepsilon}_{\text{ie}}^{t+\Delta t}\right)\right) \end{aligned} \tag{44}$$

If $\Delta\overline{\sigma}_i^{\text{NR}}$ is the NR correction from the ith iteration of Level 2, then the maximum allowable correction $\Delta\overline{\sigma}_i^{\max}$ is defined by the quasi-bisection rule in (45).

$$\begin{aligned} &\text{if } \Delta\overline{\sigma}_i^{\text{NR}} < 0 \Rightarrow \overline{\sigma}_{\text{upper}}^{t+\Delta t} = \overline{\sigma}_i^{t+\Delta t} \Rightarrow \Delta\overline{\sigma}_i^{\max} = \tfrac{1}{2}(\overline{\sigma}_{\text{lower}}^{t+\Delta t} - \overline{\sigma}_i^{t+\Delta t}) \\ &\text{if } \Delta\overline{\sigma}_i^{\text{NR}} > 0 \Rightarrow \overline{\sigma}_{\text{lower}}^{t+\Delta t} = \overline{\sigma}_i^{t+\Delta t} \Rightarrow \Delta\overline{\sigma}_i^{\max} = \tfrac{1}{2}(\overline{\sigma}_{\text{upper}}^{t+\Delta t} - \overline{\sigma}_i^{t+\Delta t}) \end{aligned} \tag{45}$$

If the absolute value of $\Delta\overline{\sigma}_i^{\text{NR}}$ is larger than the absolute value of $\Delta\overline{\sigma}_i^{\max}$, then the NR correction is bounded to $\Delta\overline{\sigma}_i^{\max}$. Otherwise, the NR correction is used.

Finally, $\overline{\sigma}_{i+1}^{t+\Delta t}$ is updated from above correction, i.e.

$$\overline{\sigma}_{i+1}^{t+\Delta t} = \overline{\sigma}_i^{t+\Delta t} + \Delta\overline{\sigma}_i^{t+\Delta t} \tag{46}$$

The advantage of the local Bounded NR method versus the full local NR method in solving the Level 2 equation is illustrated graphically in Figure 2. In this particular case, the local full NR method is diverging.

5.1.2. Nemat-Nasser solution of a pair of scalar equations. Nemat-Nasser and Li [38] and Nemat-Nasser and Chung [39] developed an explicit constitutive algorithm for their isothermal unified model. They observed that most of the deformation in incremental inelastic deformation is due to plastic flow with very small elastic deformation. Therefore, at the beginning of each increment the scalar measure of the total deformation rate can be approximated, with little error, to be due to inelastic deformation.

The appealing aspect of this method is its explicit nature, which unlike bounded NR method, means that no iterations are required at the local integration level.

By defining the initial inelastic strain rate $\dot{\overline{\varepsilon}}_{\text{ie}}^{t+\Delta t0}$ to equal the total strain rate in Equation (47)

$$\dot{\overline{\varepsilon}}_{\text{ie}}^{t+\Delta t0} = \frac{\overline{\sigma}^{*t+\Delta t} - \overline{\sigma}^{t}}{3\mu^{t+\Delta t}\Delta t} \tag{47}$$

Equation (37) can be written as

$$\overline{\sigma}^{t+\Delta t} - \overline{\sigma}^{t} = 3\mu^{t+\Delta t}\Delta t\,(\dot{\overline{\varepsilon}}_{\text{ie}}^{t+\Delta t0} - \dot{\overline{\varepsilon}}_{\text{ie}}^{t+\Delta t}) \tag{48}$$

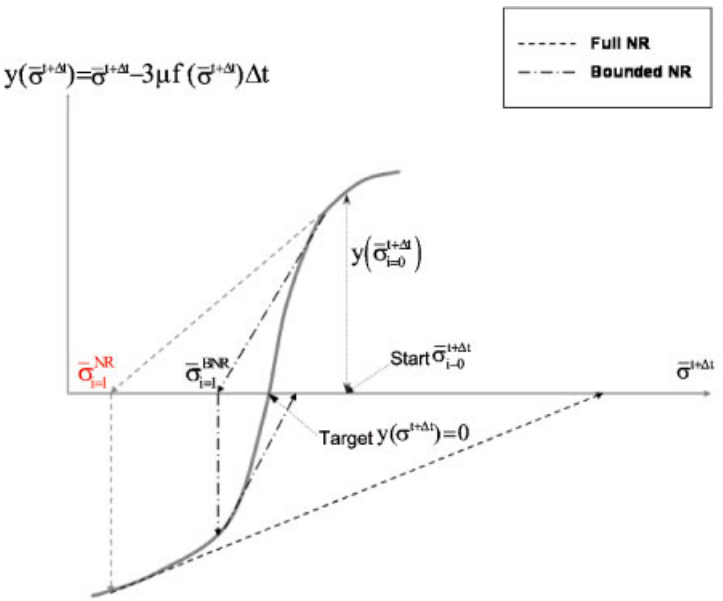

Figure 2. Bounded NR method.

Initial approximations of the effective inelastic strain and effective stress from Equations (36) and (42) are given by

$$\bar{\varepsilon}_{\mathrm{ie}}^{t+\Delta t0} = \bar{\varepsilon}_{\mathrm{ie}}^{t} + \dot{\bar{\varepsilon}}_{\mathrm{ie}}^{t+\Delta t0}\Delta t \tag{49}$$

$$\bar{\sigma}^{t+\Delta t0} = f^{-1}(\dot{\bar{\varepsilon}}_{\mathrm{ie}}^{t+\Delta t0}, \bar{\varepsilon}_{\mathrm{ie}}^{t+\Delta t0}) \tag{50}$$

Function f^{-1} can be approximated at time $t+\Delta t$ by a truncated Taylor series with initial values from Equations (48) and (49).

$$\bar{\sigma}^{t+\Delta t} = \bar{\sigma}^{t+\Delta t0} + \left.\frac{\partial f^{-1}}{\partial \dot{\bar{\varepsilon}}_{\mathrm{ie}}}\right|_0 (\dot{\bar{\varepsilon}}_{\mathrm{ie}}^{t+\Delta t} - \dot{\bar{\varepsilon}}_{\mathrm{ie}}^{t+\Delta t0}) + \left.\frac{\partial f^{-1}}{\partial \bar{\varepsilon}_{\mathrm{ie}}}\right|_0 (\bar{\varepsilon}_{\mathrm{ie}}^{t+\Delta t0} - \bar{\varepsilon}_{\mathrm{ie}}^{t+\Delta t}) \tag{51}$$

Solving Equations (36), (48), (49), and (51) together for $\bar{\sigma}^{t+\Delta t}$ and $\bar{\varepsilon}_{\mathrm{ie}}^{t+\Delta t}$ gives

$$\bar{\sigma}^{t+\Delta t} = \frac{\gamma\bar{\sigma}^{t} + \bar{\sigma}^{t+\Delta t0}}{1+\gamma} \tag{52}$$

$$\bar{\varepsilon}_{\mathrm{ie}}^{t+\Delta t} = \bar{\varepsilon}_{\mathrm{ie}}^{t} + \dot{\bar{\varepsilon}}_{\mathrm{ie}}^{t+\Delta t0}\Delta t - \frac{\bar{\sigma}^{t+\Delta t0} - \bar{\sigma}^{t}}{3\mu^{t+\Delta t}(1+\gamma)} \tag{53}$$

where

$$\gamma = \left(\left.\frac{\partial f^{-1}}{\partial \dot{\bar{\varepsilon}}_{\mathrm{ie}}}\right|_0 \frac{1}{\Delta t} + \left.\frac{\partial f^{-1}}{\partial \bar{\varepsilon}_{\mathrm{ie}}}\right|_0 \right) \frac{1}{3\mu^{t+\Delta t}} \tag{54}$$

Equations (47), (49), (50), (52)–(54) give an approximate explicit solution of a pair of integrated scalar equations (36) and (37).

If the material response is essential elastic, which is given by condition $\bar{\varepsilon}_{\text{ie}}^{t+\Delta t} < \bar{\varepsilon}_{\text{ie}}^{t}$, the alternative solution suggested by Nemat-Nasser and Li [38] and Nemat-Nasser and Chung [39] is

$$\bar{\sigma}^{t+\Delta t} = \bar{\sigma}^{*t+\Delta t} - 3\mu^{t+\Delta t} f(T^{t+\Delta t}, \bar{\sigma}^{t}, \bar{\varepsilon}_{\text{ie}}^{t}, \%\text{C})\Delta t \tag{55}$$

$$\bar{\varepsilon}_{\text{ie}}^{t+\Delta t} = \bar{\varepsilon}_{\text{ie}}^{t} + f(T^{t+\Delta t}, \bar{\sigma}^{t}, \bar{\varepsilon}_{\text{ie}}^{t}, \%\text{C})\Delta t \tag{56}$$

6. TREATMENT OF LIQUID/MUSHY ZONE

In this model, elements containing both liquid and solid are generally given no special treatment regarding either material properties or finite element assembly. The only difference is to choose a constitutive law that enforces negligible liquid strength and stress when the current temperature is higher than the solidus temperature. This fixed-grid approach avoids difficulties of adaptive meshing or 'giving birth' to solid elements as used in Reference [40].

Two different approaches are implemented:

- Elastic-perfectly plastic rate-independent model with small yield stress.
- Extremely rapid creep rate function in the liquid/mushy zone.

6.1. Elastic-perfectly plastic model in liquid/mushy zone

The first approach implements an isotropic elastic-perfectly plastic rate-independent model for liquid or mushy elements, defined when $T > T_{\text{sol}}$ for at least one material point. The yield stress $\sigma_{\text{Y}} = 0.03\,\text{MPa}$ is chosen small enough to effectively eliminate stresses in the liquid-mushy zone, but also large enough to avoid computational difficulties. These liquid/mushy elements use the standard radial-return algorithm, which is a special form of backward-Euler procedure [29, 32, 41].

The algebraic equations associated with integrating the model are developed here for a single variable, equivalent inelastic (plastic) strain increment $\Delta\bar{\varepsilon}_{\text{ie}}$.

Splitting the stress update into volumetric and deviatoric parts [32] gives

$$\sigma_{ij}^{t+\Delta t} = \frac{1}{3}\sigma_{kk}^{t+\Delta t}\delta_{ij} + \sigma_{ij}^{\prime t+\Delta t} = \frac{1}{3}\sigma_{kk}^{*t+\Delta t}\delta_{ij} + \left(1 - \frac{3\mu\Delta\lambda}{\bar{\sigma}^{*t+\Delta t}}\right)\sigma_{ij}^{\prime *t+\Delta t} \tag{57}$$

$\boldsymbol{\sigma}^{*t+\Delta t}$ is elastic stress predictor given by

$$\boldsymbol{\sigma}^{*t+\Delta t} = \boldsymbol{\sigma}^{t} + \underline{\underline{\mathbf{D}}} : \Delta\hat{\boldsymbol{\varepsilon}}^{t+\Delta t} \tag{58}$$

μ is the shear modulus, and $\Delta\lambda$ is a plastic strain multiplier, which equals $\Delta\bar{\varepsilon}_{\text{ie}}$ for the von Mises yield criterion. Equating the volumetric components, $\sigma_{kk}^{*t+\Delta t} = \sigma_{kk}^{t+\Delta t}$, Equation (57) simplifies to relate the deviatoric stress components as follows:

$$\sigma_{ij}^{\prime t+\Delta t} = \eta\sigma_{ij}^{\prime *t+\Delta t} = \left(1 - \frac{3\mu\Delta\bar{\varepsilon}_{\text{ie}}^{t+\Delta t}}{\bar{\sigma}^{*t+\Delta t}}\right)\sigma_{ij}^{\prime *t+\Delta t} \tag{59}$$

These deviatoric stresses must satisfy the von Mises yield criterion given by yield function g

$$g^{t+\Delta t} = \overline{\sigma}^{t+\Delta t}(\boldsymbol{\sigma}'^{t+\Delta t}) - \sigma_{\mathrm{Y}}^{t+\Delta t}(\overline{\varepsilon}_{\mathrm{ie}}^{t+\Delta t}) = \eta\overline{\sigma}^{*t+\Delta t} - \sigma_{\mathrm{Y}}^{t+\Delta t}(\overline{\varepsilon}_{\mathrm{ie}}^{t+\Delta t}) = 0 \tag{60}$$

For nonlinear hardening, $\mathrm{HR} = \partial\sigma_{\mathrm{Y}}/\partial\overline{\varepsilon}_{\mathrm{ie}}$ is not constant, so Equation (60) is nonlinear and can be solved for $\Delta\overline{\varepsilon}_{\mathrm{ie}}^{t+\Delta t}$ by the full NR method. For the present perfect plasticity, $\mathrm{HR} = 0$, and (60) gives the simple solution for $\Delta\overline{\varepsilon}_{\mathrm{ie}}^{t+\Delta t}$

$$\Delta\overline{\varepsilon}_{\mathrm{ie}}^{t+\Delta t} = \frac{\overline{\sigma}^{*t+\Delta t} - \sigma_{\mathrm{Y}}}{3\mu} \tag{61}$$

At the beginning of every increment, a trial stress (elastic predictor) $\boldsymbol{\sigma}^{*t+\Delta t}$ is calculated from (58). $\overline{\sigma}^{*t+\Delta t}$ is then calculated from (18) and (17) and compared with $\sigma_{\mathrm{Y}}^{t}(\varepsilon_{\mathrm{ie}}^{t})$. If $\overline{\sigma}^{*t+\Delta t} < \sigma_{\mathrm{Y}}^{t}$ only elastic response is calculated. Otherwise if $\overline{\sigma}^{*t+\Delta t} \geqslant \sigma_{\mathrm{Y}}^{t}$, the material yields and $\Delta\overline{\varepsilon}_{\mathrm{ie}}^{t+\Delta t}$ is either solved from (60) for a material with hardening, or calculated directly from (61) for perfect plasticity. Once $\Delta\overline{e}_{\mathrm{ie}}^{t+\Delta t} = \Delta\lambda$ is found, $\boldsymbol{\sigma}^{t+\Delta t}$ is given from (57), and $\Delta\boldsymbol{\varepsilon}_{\mathrm{ie}}^{t+\Delta t}$ is calculated from the flow rule, given by the Prandtl–Reuss equation [26]

$$(\Delta\varepsilon_{\mathrm{ie}}^{t+\Delta t})_{ij} = \frac{3}{2}\frac{\sigma_{ij}'^{t+\Delta t}}{\overline{\sigma}^{t+\Delta t}}\Delta\overline{\varepsilon}_{\mathrm{ie}}^{t+\Delta t} \tag{62}$$

Finally, plastic strains at the end of the increment $\boldsymbol{\varepsilon}_{\mathrm{ie}}^{t+\Delta t}$ are updated.

The consistent tangent operator (Jacobian), consistent with the backward-Euler integration, provides a quadratic convergence of the global equilibrium equations when using the NR method [31, 32].

$$\underline{\underline{\mathbf{J}}} = \left(k_{\mathrm{B}} - \frac{2\mu\eta}{3}\right)(\mathbf{I}\otimes\mathbf{I}) + 2\mu(\eta\underline{\underline{\mathbf{I}}} - \beta\boldsymbol{\sigma}'^{*t+\Delta t}\otimes\boldsymbol{\sigma}'^{*t+\Delta t}) \tag{63}$$

where $\underline{\underline{\mathbf{I}}}$ and $\mathbf{I}$ are, respectively, fourth- and second-order identity tensors and

$$k_{\mathrm{B}} = \frac{E}{3(1-2\upsilon)} \quad \text{(bulk modulus)} \tag{64}$$

$$\beta = \frac{3}{2(\overline{\sigma}^{*t+\Delta t})^2}(1-\eta)\left(1 - \frac{\overline{\sigma}^{*t+\Delta t}}{\Delta\lambda(3\mu + \mathrm{HR}^{t+\Delta t})}\right) \tag{65}$$

6.2. Rapid creep rate function in liquid/mushy zone

An alternative way to treat liquid and mushy material is to create a viscoplastic constitutive relation that acts as a penalty function to generate inelastic strain in proportion of the absolute difference between equivalent stress $\overline{\sigma}$ and a small yield stress σ_{Y} [2–4].

$$\dot{\overline{\varepsilon}}_{\mathrm{ie}} = \begin{cases} \dfrac{c_S}{\mu_V}(|c_S\overline{\sigma}| - \sigma_{\mathrm{Y}}), & |c_S\overline{\sigma}| > \sigma_{\mathrm{Y}} \\ 0, & |c_S\overline{\sigma}| \leqslant \sigma_{\mathrm{Y}} \end{cases} \tag{66}$$

c_S is a sign defined in Equation (20), while the parameter μ_V^{-1} is a large number. For large values of μ_V^{-1}, which physically match the reciprocal of the viscosity of molten steel $1.5\times10^8\,\mathrm{MPa^{-1}\,s^{-1}}$, numerical difficulties were experienced with Abaqus global NR equilibrium iterations even when using the robust local viscoplastic scheme from Section 4. Thus, much smaller numbers for μ_V^{-1} had to be chosen that were still able to enforce negligible strength and stress in mushy/liquid zone and produce accurate stress results. The CON2D model handles large μ_V^{-1} without problem. In alloy systems with large mushy zones, the restriction of flow through the dendrite network could generate both stress and hot tearing in the mushy zone [42]. This behaviour can be taken into account in this model by choosing the value of μ_V according to the actual permeability of the mushy zone. Further details on this idea are given elsewhere [2].

7. SUMMARY OF LOCAL INTEGRATION ALGORITHM APPLIED IN UMAT

Starting from an equilibrium at some time t, Abaqus provides subroutine UMAT with time increment Δt, stress vector $\{\sigma\}^t$, total mechanical strain vector $\{\varepsilon\}^t$, inelastic strain vector $\{\varepsilon_{\mathrm{ie}}^t\}$ (which is supplied via the array of state variables STATEV), and an initial guess for total mechanical strain increment vector $\{\Delta\hat{\varepsilon}\}^{t+\Delta t}$ calculated from current displacement increments, see Figure 1. Thermal strains at time t, $\{\varepsilon_{\mathrm{th}}\}^t$, and increments of thermal strains $\{\Delta\varepsilon_{\mathrm{th}}\}^{t+\Delta t}$ are computed from the previous transient heat transfer analysis and subtracted from $\{\varepsilon\}^t$ and $\{\Delta\hat{\varepsilon}\}^{t+\Delta t}$, respectively, see Equation (34).

The subroutine UMAT has then to supply Abaqus with a stress vector $\{\sigma^{t+\Delta t}\}$, updated according to the constitutive laws, and the consistent tangent operator defined in Equation (27). An accurate Jacobian (CTO) is essential to achieve fast quadratic convergence in the global NR iterations [31]. Also, the updated inelastic strain vector $\{\varepsilon_{\mathrm{ie}}\}^{t+\Delta t}$ is carried to the next iteration via updated STATEV array [28].

If the current temperature exceeds T_{sol}, the material point still contains liquid, so the elastic-perfectly plastic algorithm from Section 6.1 may be used. If Equation (66) is used for the liquid, or if the material point is solid, then the following six steps are used for time integration of the elastic-viscoplastic constitutive law, given in the form of Equation (16) for the inelastic strain rate.

Step 1: Calculation of equivalent stress and equivalent inelastic strain at time t.

$$\overline{\sigma}^t=\frac{1}{\sqrt{2}}\sqrt{(\sigma_x^t-\sigma_y^t)^2+(\sigma_y^t-\sigma_z^t)^2+(\sigma_z^t-\sigma_x^t)^2+6((\sigma_{xy}^t)^2+(\sigma_{yz}^t)^2+(\sigma_{zx}^t)^2)} \tag{67}$$

$$\overline{\varepsilon}_{\mathrm{ie}}^t=\frac{\sqrt{2}}{3}\sqrt{(\varepsilon_{\mathrm{ie}x}^t-\varepsilon_{\mathrm{ie}y}^t)^2+(\varepsilon_{\mathrm{ie}y}^t-\varepsilon_{\mathrm{ie}z}^t)^2+(\varepsilon_{\mathrm{ie}z}^t-\varepsilon_{\mathrm{ie}x}^t)^2+6((\varepsilon_{\mathrm{ie}xy}^t)^2+(\varepsilon_{\mathrm{ie}yz}^t)^2+(\varepsilon_{\mathrm{ie}zx}^t)^2)} \tag{68}$$

Step 2: Calculation of trial stress vector $\{\sigma^*\}^{t+\Delta t}$, deviatoric trial stress vector $\{\sigma'^*\}^{t+\Delta t}$, and equivalent trial stress $\overline{\sigma}^{*t+\Delta t}$.

$$\{\sigma^*\}^{t+\Delta t}=[D]^{t+\Delta t}(\{\varepsilon\}^t-\{\varepsilon_{\mathrm{ie}}\}^t+\{\Delta\hat{\varepsilon}\}^{t+\Delta t}) \tag{69}$$

$$\{\sigma'^*\}^{t+\Delta t}=\{\sigma^*\}^{t+\Delta t}-\tfrac{1}{3}(\sigma_x^{*t+\Delta t}+\sigma_y^{*t+\Delta t}+\sigma_z^{*t+\Delta t})\{1,1,1,0,0,0\}^{\mathrm{T}} \tag{70}$$

$$\overline{\sigma}^{*t+\Delta t}=\frac{1}{\sqrt{2}}\sqrt{(\sigma_x^{*t+\Delta t}-\sigma_y^{*t+\Delta t})^2+(\sigma_y^{*t+\Delta t}-\sigma_z^{*t+\Delta t})^2+(\sigma_z^{*t+\Delta t}-\sigma_x^{*t+\Delta t})^2+6((\sigma_{xy}^{*t+\Delta t})^2+(\sigma_{yz}^{*t+\Delta t})^2+(\sigma_{zx}^{*t+\Delta t})^2)} \tag{71}$$

Step 3: Solve a pair of scalar nonlinear equations (36) and (37) for $\overline{\sigma}^{t+\Delta t}$ and $\overline{\varepsilon}_{\mathrm{ie}}^{t+\Delta t}$ by using methods from 5.1.1 or 5.1.2.

Step 4: Calculate radial-return factor $\eta^{t+\Delta t}$, expand stress vector $\{\sigma\}^{t+\Delta t}$, calculate $\{\sigma'\}^{t+\Delta t}$

$$\eta^{t+\Delta t}=\frac{\overline{\sigma}^{t+\Delta t}}{\overline{\sigma}^{*t+\Delta t}} \tag{72}$$

$$\{\sigma\}^{t+\Delta t}=\eta^{t+\Delta t}\{\sigma'^{*}\}^{t+\Delta t}+\tfrac{1}{3}(\sigma_x^{*t+\Delta t}+\sigma_y^{*t+\Delta t}+\sigma_z^{*t+\Delta t})\{1\ \ 1\ \ 1\ \ 0\ \ 0\ \ 0\}^{\mathrm{T}} \tag{73}$$

$$\{\sigma'\}^{t+\Delta t}=\{\sigma\}^{t+\Delta t}-\tfrac{1}{3}(\sigma_x^{t+\Delta t}+\sigma_y^{t+\Delta t}+\sigma_z^{t+\Delta t})\{1\ \ 1\ \ 1\ \ 0\ \ 0\ \ 0\}^{\mathrm{T}} \tag{74}$$

Step 5: Calculate increments of inelastic strains from Prandtl–Reuss flow law, update the inelastic strains and store them in STATEV array.

$$\{\Delta\varepsilon_{\mathrm{ie}}\}^{t+\Delta t}=\frac{3}{2}\frac{\{\sigma'\}^{t+\Delta t}}{\overline{\sigma}^{t+\Delta t}}\Delta\overline{\varepsilon}_{\mathrm{ie}}^{t+\Delta t} \tag{75}$$

$$\{\varepsilon_{\mathrm{ie}}\}^{t+\Delta t}=\{\varepsilon_{\mathrm{ie}}\}^{t}+\{\Delta\varepsilon_{\mathrm{ie}}\}^{t+\Delta t} \tag{76}$$

Step 6: Calculate Jacobian (consistent tangent operator).

The derivation of the Jacobian for this form of constitutive laws is given in Reference [25]. The final expression is given in Equation (77) in tensor notation.

$$\underline{\underline{\mathbf{J}}}^{t+\Delta t}=2\mu^{t+\Delta t}\eta^{t+\Delta t}\underline{\underline{\mathbf{I}}}+\left(\kappa^{t+\Delta t}-\frac{2\mu^{t+\Delta t}\eta^{t+\Delta t}}{3}\right)\mathbf{I}\otimes\mathbf{I}$$
$$-2\mu^{t+\Delta t}(\eta^{t+\Delta t}-c_J^{t+\Delta t})\mathbf{N}^{t+\Delta t}\otimes\mathbf{N}^{t+\Delta t} \tag{77}$$

The above variables were defined except normal flow tensor $\mathbf{N}$ and constant c_J

$$\mathbf{N}^{t+\Delta t}=\sqrt{\frac{3}{2}}\frac{\boldsymbol{\sigma}'^{t+\Delta t}}{\overline{\sigma}^{t+\Delta t}} \tag{78}$$

$$c_J^{t+\Delta t}=\frac{1-\dot{\overline{\varepsilon}}_{\mathrm{ie}}^{t+\Delta t}\Delta t}{1+\Delta t(3\mu^{t+\Delta t}(\partial\dot{\overline{\varepsilon}}_{\mathrm{ie}}/\partial\overline{\sigma})-(\partial\dot{\overline{\varepsilon}}_{\mathrm{ie}}/\partial\overline{\varepsilon}_{\mathrm{ie}}))} \tag{79}$$

The derivatives in (79) are found from the strain rate laws given in Equations (66) or (16) evaluated at $t+\Delta t$.

8. 2D PROBLEMS

In many solidification processes, such as the continuous casting of steel, one dimension of the casting is much longer than the others, and is otherwise unconstrained. In this case, it is quite reasonable to apply a condition of generalized plane strain in the long direction (z), and to solve a 2D thermal stress problem in the transverse (x–y) plane. This condition reasonably allows a 2D computation to produce the complete 3D stress state in the plane section.

The generalized plane strain condition assumes that strain in the undiscretized longitudinal direction z is a linear function of the in-plane coordinates:

$$\varepsilon_{zz} = a + bx + cy \tag{80}$$

The unknown constants (a, b, c) are solved together with the in-plane displacements, adding three extra degrees of freedom to the global system of equations for the entire domain. The associated additional equation for a is

$$\int \sigma_{zz} \, \mathrm{d}A = F_z \tag{81}$$

where F_z is an external mechanical force acting in the z direction. The two additional equations for b and c are

$$\int \sigma_{zz} y \, \mathrm{d}A = M_x \tag{82}$$

$$\int \sigma_{zz} x \, \mathrm{d}A = M_y \tag{83}$$

where M_x, M_y are external mechanical moments in the x and y directions, respectively.

A simplification of this condition occurs when two-fold symmetry causes the axial strain to be a constant ($\varepsilon_{zz} = a$). In this case, M_x, M_y, b and c all equal zero, and only one additional global equation must be solved for a. Furthermore, the axial force, F_z is set to zero, when there is no axial load or constraint. The axial strain, a, is generally negative for solidification problems, as it accounts for the average thermal shrinkage of the plane section.

9. MODEL VALIDATION

A semi-analytical solution of thermal stress in an unconstrained solidifying plate, derived by Weiner and Boley [1] is used here as an ideal validation problem for solidification stress models. This 1D solution takes advantage of the large length and width of the casting. Thus, it is reasonable to apply the generalized plane strain condition, discussed in the previous section, in both the y and z directions, to produce the complete 3D stress and strain state.

The domain adopted for this problem is a thin slice through the plate thickness using 2D generalized plane strain elements (in the axial z direction) with zero relative rotation (i.e. $b = c = 0$ in Equation (80)). The domain moves with the strand in a Langrangian frame of reference as shown in Figure 3. In addition, a second generalized plane strain condition was imposed in the y direction (parallel to the surface) by coupling the displacements of all nodes

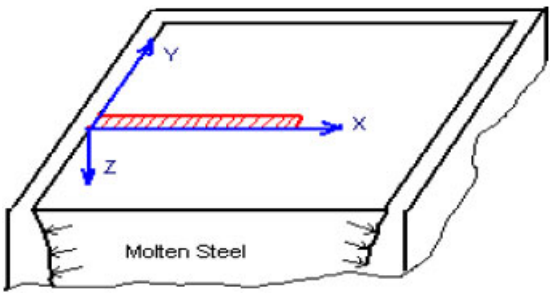

Figure 3. Solidifying slice.

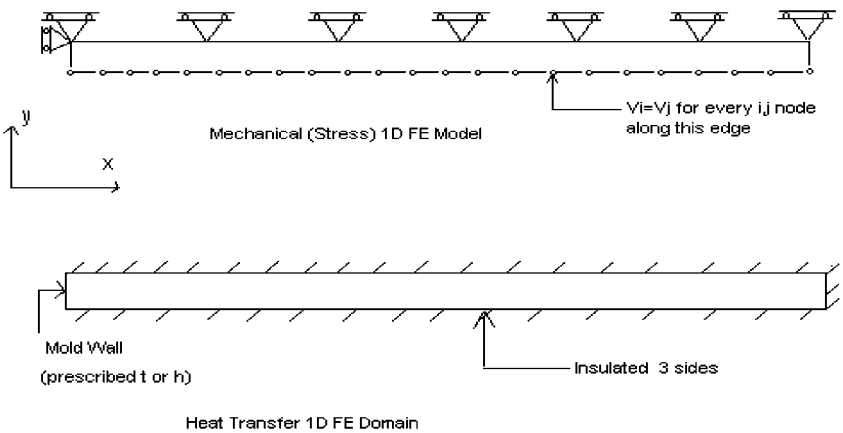

Figure 4. Mechanical and thermal FE domains.

along the bottom edge of the slice domain as shown in Figure 4. This was accomplished using the *EQUATION option in abaqus [28]. The normal (x) displacement of all nodes along the bottom edge of the domain is fixed to zero. Tangential stress was left equal zero along all surfaces. Finally, the ends of the domain are constrained to remain vertical, which prevents any bending in the xy plane.

The material in this problem has elastic-perfectly plastic constitutive behaviour. The yield stress drops linearly with temperature from 20 MPa at 1000°C to zero at the solidus temperature 1494.4°C, which was approximated by 0.03 MPa at the solidus temperature. A very narrow mushy region, 0.1°C, is used to approximate the single melting temperature assumed by Boley and Weiner. All the constants used in this solidification model are listed in Table I.

Abaqus with UMAT is tested with both elastic-perfectly plastic algorithm from Section 6.1, and a robust viscoplastic algorithms from Section 5 applied to the rapid liquid strain function equation (35) to emulate elastic-perfectly plastic behaviour. Also, an in-house code, CON2D [2–4] code is used to solve this problem as well as the realistic problem from Section 10. In the latter elastic-viscoplastic model, the constitutive relation was transformed into a computationally more challenging form, the highly nonlinear creep function of Equation (66) with $\mu_V^{-1} = 1.5 \times 10^8\,\mathrm{MPa}^{-1}\,\mathrm{s}^{-1}$ and $\sigma_Y = 0.01\,\mathrm{MPa}$ in the liquid.

Table I. Constants used in solidification test problem.

Conductivity (W/m K)	33.0
Specific heat (J/kg K)	661.0
Elastic modulus in solid (GPa)	40.0
Elastic modulus in liquid (GPa)	14.0
Thermal linear expansion coefficient (1/K)	0.00002
Density (kg/m^3)	7500.
Poisson's ratio	0.3
Liquidus temperature (°C)	1494.45
Fusion temperature (analytical) (°C)	1494.4
Solidus temperature (°C)	1494.35
Initial temperature (°C)	1495.0
Latent heat (J/kg K)	272 000.0
Reciprocal of liquid viscosity (MPa^{-1} s^{-1})	1.5×10^8
Surface film coefficient (W/m^2 K)	250 000

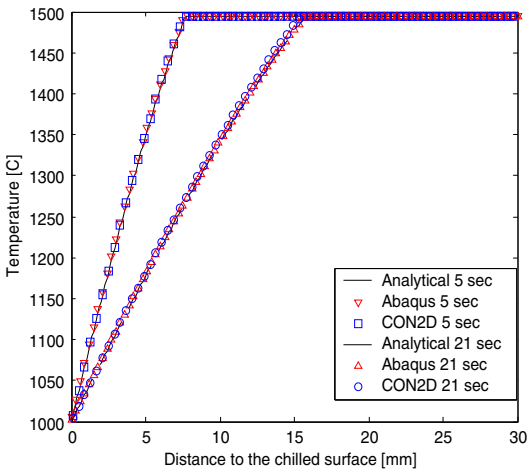

Figure 5. Temp. distribution along the solidifying slice.

Figure 4 shows the domain and boundary conditions for both the heat transfer and mechanical models. Heat transfer analysis is run first to get the temporal and spatial temperature field. Stress analysis is then run using this temperature field. The domain in Abaqus has a single row of 300 plane four-node elements in both thermal and stress analysis. CON2D uses a similarly refined mesh with six-node, quadratic triangular elements.

Figures 5 and 6 show the temperature and the stress distribution across the solidifying shell at two different solidification times. The semi-analytical solutions were computed with MATLAB by Li and Thomas [2]. The almost-linear temperature gradient through the shell gradually drops as solidification proceeds. This faster cooling of the interior relative to the surface region naturally causes interior contraction and tensile stress, which is offset by compression at the surface. The changes in slope at ~ -15 and $+12$ MPa denote the transition from the elastic

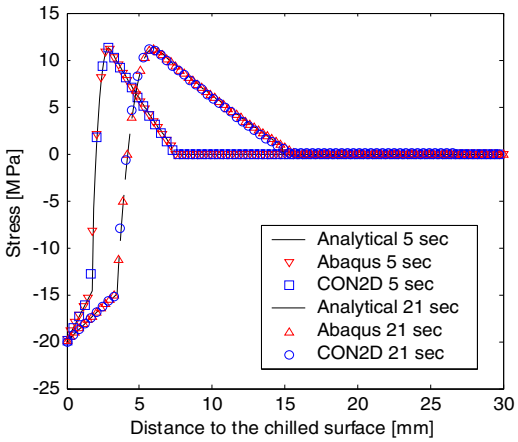

Figure 6. Y and Z stress distributions along the solidifying slice.

central region to the plastically yielded surface and interior. Both lateral stress distributions (y and z directions) are the same for both codes, which is expected from the identical boundary conditions in these two directions. Shear stresses and x-stress are all zero. Identical results were found with the perfectly plastic and the viscoplastic liquid functions coded in UMAT, so there is a single Abaqus curve representation on the graphs. The original boundary condition prescribed an abrupt surface quench to 1000°C, which causes convergence problems for Abaqus at early times. Instead applying a convection boundary condition with a film coefficient of $250\,000\,\mathrm{W/m^2C}$ alleviated the convergence problems and improved the stress results (under 1% error). CON2D produced similar accuracy with the semi-analytical solution.

CPU times were also similar between CON2D and Abaqus with the elastic-perfectly plastic (radial return) algorithm. The viscoplastic algorithms from Section 5.1 coded in Abaqus were ~ 10 times slower, and experienced computational difficulties, which required lower μ_V^{-1}, and resulted in $\sim 4\%$ error.

The two CREEP methods supported in Abaqus [28, 35] were also tested for this problem using a less nonlinear form of Equation (66) with smaller μ_V^{-1}. The implicit CREEP method always failed to converge despite many attempts, even when used in conjuction with Abaqus built-in plasticity algorithm based on classic radial-return method (Section 6.1) for an elastic-perfectly plastic liquid/mushy zone. The explicit CREEP also experienced convergence problems, but did converge with the easier, but less accurate lower μ_V^{-1} equation. Although the stress results were comparable, the CPU times with explicit creep were ~ 20 times larger compared to Abaqus with the UMAT of this work or CON2D.

Abaqus automatically adjusts the time increment size, based on the convergence criteria from the previous time increment [28], starting from an initial time increment of 10^{-5} at 0 s, and increasing to 0.3 s after 15 s. Time increments are specified manually in CON2D to increase logarithmically from 0.001 s at 0 s to 0.1 s at 21 s. A formal study of mesh and time increment refinement was conducted for CON2D by Zhu [3], which shows that the 300-node mesh used here is more than sufficient to achieve accuracy within 1% error with a fixed time increment of 0.01 s (1000 time increments per 10 s), Figure 7. Further convergence studies with CON2D

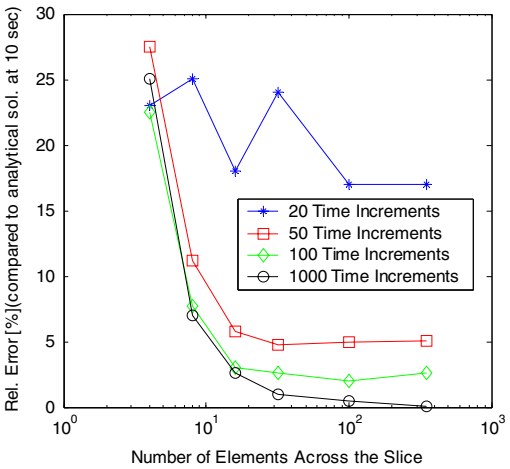

Figure 7. CON2D convergence study [3].

for this problem were performed by Li and Thomas [2], including variable mesh and time increment sizes.

10. ANALYSIS OF SOLIDIFYING SLICE IN CONTINUOUS CASTING MOLD

The FE model of solidification of a slice, with the identical mesh of nodes and elements that was validated in the previous section, was next applied to a realistic problem of continuous casting of steel with temperature-dependent properties and boundary conditions matching typical plant conditions. The artificial surface-quenching condition was replaced with an instantaneous interfacial heat flux profile that varied with time down the mold according to mold thermocouple measurements [2] and is given in Equation (84), and Figure 8. This heat flux boundary condition was input to Abaqus using the DFLUX subroutine.

$$\hat{q}(\mathrm{MW/m^2}) = 6.5(t\ (s) + 1)^{-1/2} \tag{84}$$

Constitutive equation (16) was chosen for solidifying plain-carbon steel in the austenite phase using the rate-dependent, elastic-visco-plastic model III of Kozlowski *et al.* [43] given in Equation (85). This model was developed to match tensile test measurements of Wray [44] and creep test data of Suzuki *et al.* [45]

$$\dot{\bar{\varepsilon}}_{\mathrm{ie}}\ (\mathrm{s}^{-1}) = f_C(\bar{\sigma}\ (\mathrm{MPa}) - f_1\bar{\varepsilon}_{\mathrm{ie}}|\bar{\varepsilon}_{\mathrm{ie}}|^{f_2-1})^{f_3}\ \exp\left(-\frac{Q}{T\ (\mathrm{K})}\right)$$

where

$$Q = 44\,465$$

$$f_1 = 130.5 - 5.128 \times 10^{-3} T\ \ (\mathrm{K})$$

$$f_2 = -0.6289 + 1.114 \times 10^{-3} T\ \ (\mathrm{K})$$

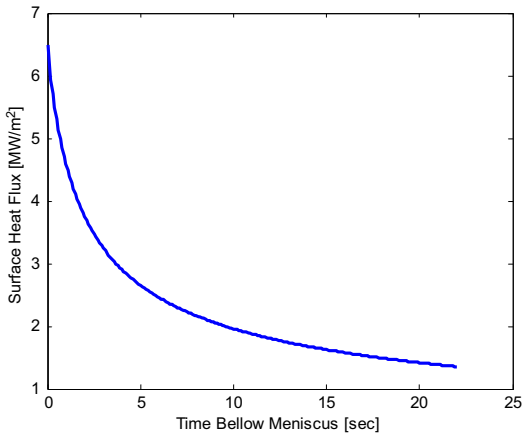

Figure 8. Instantaneous interfacial heat flux.

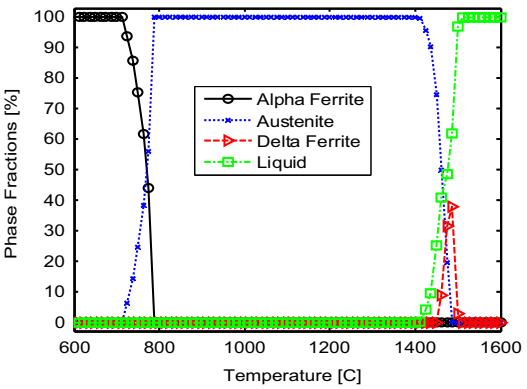

Figure 9. Phase fractions for 0.27%C carbon steel [2].

$$f_3 = 8.132 - 1.54 \times 10^{-3} T \ \ (\mathrm{K})$$

$$f_C = 46\,550 + 71\,400(\%\mathrm{C}) + 12\,000 \ \ (\%\mathrm{C})^2 \tag{85}$$

This empirical relation relates the equivalent inelastic strain rate $\dot{\bar{\varepsilon}}_{\mathrm{ie}}$ with the von mises stress $\bar{\sigma}$, equivalent inelastic strain $\bar{\varepsilon}_{\mathrm{ie}}$, activation constant Q, steel grade %C, and several empirical temperature- or steel-grade-dependent constants f_1, f_2, f_3, f_C.

Temperature-dependent properties were chosen for 0.27%C plain-carbon steel with $T_{\mathrm{sol}} = 1411.79°\mathrm{C}$ and $T_{\mathrm{liq}} = 1500.72°\mathrm{C}$. All temperature-dependent material property calculations are an integral part of the CON2D code [2–4], and were extracted for Abaqus input. Figure 9 shows the fractions of solid phases and liquid for this steel [2], which confirms the assumption of single-phase austenite for the solid over the temperature range of interest.

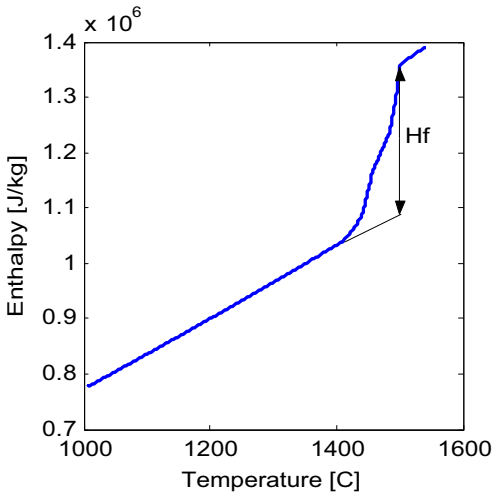

Figure 10. Enthalpy for 0.27%C plain carbon steel.

The enthalpy curve used to relate heat content and temperature in this study, $H(T)$, is shown in Figure 10. It was obtained by integrating the specific heat curve fitted from measured data of Pehlke *et al.* [46]. Abaqus tracks the latent heat $Hf = 257\,867\,\mathrm{J/kg}$ separately from the specific heat $c_p(T)$, which is found from the slope of this $H(T)$ curve, except in the solidification region, where c_p is found from [11]

$$c_p(T) = \frac{\mathrm{d}H}{\mathrm{d}T} - \frac{Hf}{(T_{\mathrm{liq}} - T_{\mathrm{sol}})} \tag{86}$$

The temperature-dependent conductivity function for 0.27%C plain-carbon steel is fitted from measured data by Harste [47], and given in Figure 11. The conductivity increases in the liquid region by a factor of 6.65 to partly account for the effect of convection due to flow in the liquid steel pool [48]. Density was assumed constant at this work, $7400\,\mathrm{kg/m^3}$, in order to maintain constant mass.

Thermal strain can be calculated from the temperature changes simulated by the heat transfer model and from the unified state function, thermal linear expansion (TLE), which includes the volume change of materials undergoing both temperature change and phase transformation, Figure 12 [2]. The thermal strain in CON2D is expressed by Equation (87) [2].

$$\{\varepsilon_{\mathrm{th}}\} = (\mathrm{TLE}(T) - \mathrm{TLE}(T_{\mathrm{ref}}))\{1\ \ 1\ \ 1\ \ 0\ \ 0\ \ 0\}^{\mathrm{T}} \tag{87}$$

T_{ref} is an arbitrary reference temperature, typically either T_{sol} or 20°C. This thermal linear expansion function was obtained from solid-phase density measurements compiled by Harste [47] and Harste *et al.* [49] equation (88), while in liquid/mushy zone by density measurements by Jimbo and Cramb [50].

$$\mathrm{TLE} = \sqrt[3]{\frac{\rho(T_{\mathrm{ref}})}{\rho(T)}} - 1 \tag{88}$$

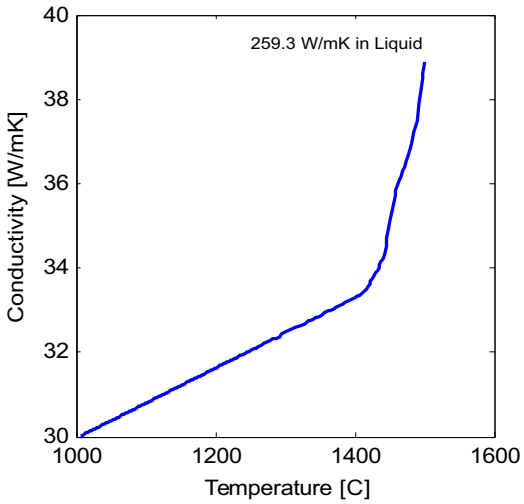

Figure 11. Thermal conductivity for 0.27%C plain carbon steel.

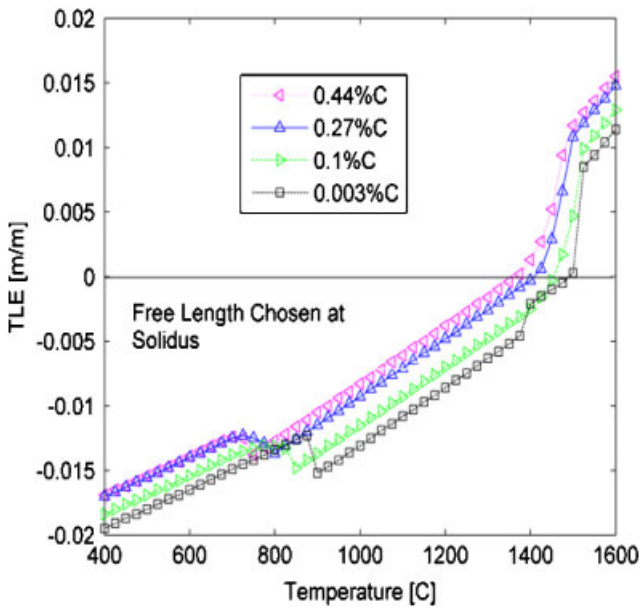

Figure 12. Thermal linear expansion (TLE) of plain carbon steels.

Abaqus calculates thermal strains from Equation (89) [28]

$$\{\varepsilon_{\text{th}}\} = (\alpha(T)(T - T_{\text{ref}}) - \alpha(T_{\text{init}})(T_{\text{init}} - T_{\text{ref}}))\{1\ \ 1\ \ 1\ \ 0\ \ 0\ \ 0\}^{\text{T}} \tag{89}$$

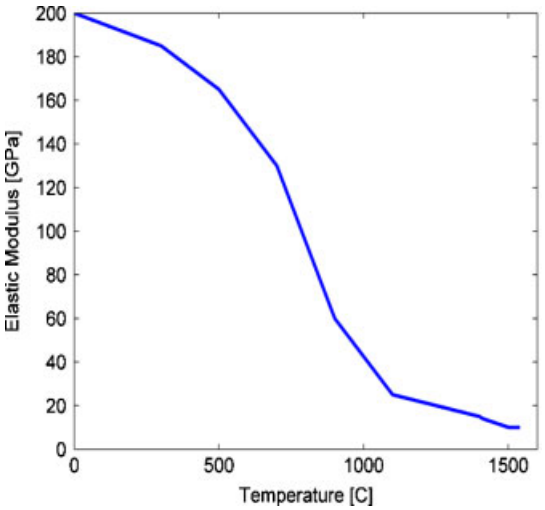

Figure 13. Elastic modulus for plain carbon steel.

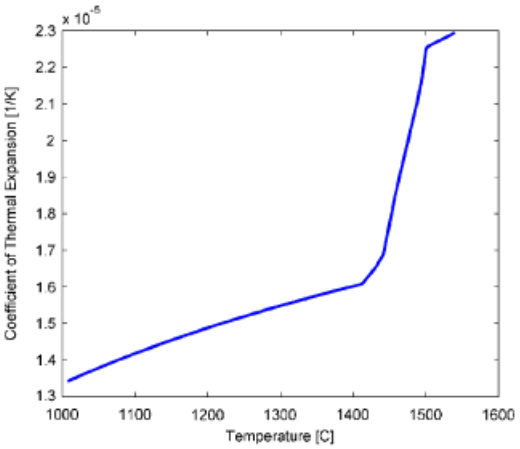

Figure 14. Coefficient of thermal linear expansion for 0.27%C plain carbon steel, $T_{\text{ref}} = 20°\text{C}$.

where $\alpha(T)$ is the temperature-dependent coefficient of thermal expansion, T_{init} is initial temperature (pouring temperature), and T_{ref} is a very important reference temperature. The following expression is used to calculate $\alpha(T)$ from TLE:

$$\alpha(T) = \frac{\text{TLE}(T_{\text{ref}}) - \text{TLE}(T)}{T_{\text{ref}} - T} \tag{90}$$

Identical thermal strain results are produced with Abaqus for $T_{\text{ref}} = T_{\text{sol}}$ and $T_{\text{ref}} = 20°\text{C}$, though $\alpha(T)$ curves have totally different shape, see Figures 14 and 15. This is a clear sign

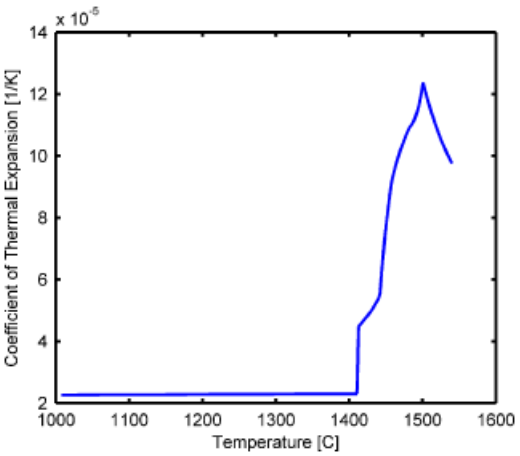

Figure 15. Coefficient of thermal linear expansion for 0.27%C plain carbon steel, $T_{\text{ref}} = T_{\text{sol}} = 1411.79°\text{C}$.

that the expression from Equation (90) is correctly calculating $\alpha(T)$ from TLE. Figure 14 has $\alpha(T)$ for $T_{\text{ref}} = 20°\text{C}$.

Elastic modulus E generally decreases as the temperature increases, although its value at high temperatures is uncertain. The temperature-dependent elastic modulus curve used in this model was fitted from measurements from Mizukami *et al.* [51] by Kozlowski *et al.* [43] as shown in Figure 13. Unlike in other models, the elastic modulus of the liquid here was given the physically realistic value of 14 GPa. This value also avoids numerical trouble from excessively small values in the stiffness matrix. Actually, the value of the elastic modulus in the liquid has little effect on the stress results, due to the negligible strength of the liquid. Poisson ratio is 0.3 constant.

A 21 s simulation was performed, which corresponds to 700 mm long shell of cast steel at a casting speed of 33.3 mm/s (2 m/min). The temperature and stress distribution results along the solidifying slice are presented at four times during solidification for both codes in Figures 16 and 17. The temperature and stress histories are given for two material points in Figures 18 and 19. Temperature and stress contours are constructed from the transient results in Figures 20 and 21, and represent the steady-state appearance of the solidifying shell. The shape of the tensile region that forms inside the shell, and the development of surface compression are clearly revealed. These stress distributions are qualitatively similar to that of the semi-analytical solution. The shape changes slightly due to the change in heat flux and properties. The temperature results predicted by Abaqus and CON2D match except near the solidification front, where an unplanned difference in phase fraction evolution causes minor variations. This causes minor variations in the stress results, although there is still a reasonable match. The operator-splitting method in CON2D produced minor oscillations in the stresses, such as the bump at ~ 1 s in Figure 19.

Detailed CPU benchmark results are presented in Table II for all combinations of methods compared. Simulations were performed on an IBM p690 with Power 4, 1.3 GHz CPU running under AIX 5.1 OS. Abaqus required 2–3 global NR iterations per increment, and 5.6 min of CPU time for the 21 s stress simulation with the elastic-perfectly plastic (radial-return) algorithm for liquid/mush. Depending on severity of the nonlinearity in the strain rate—stress function

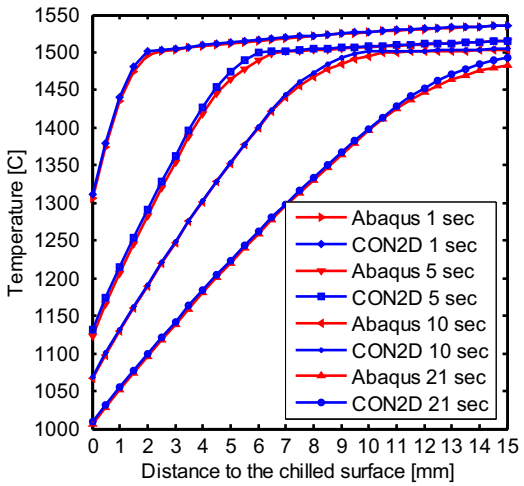

Figure 16. Temperature distribution along the solidifying slice in continuous casting mold.

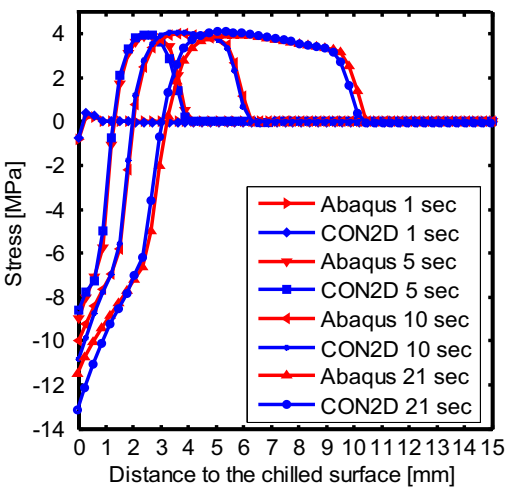

Figure 17. Lateral (y and z) stress distribution along the solidifying slice in continuous casting mold.

(i.e. value of μ_V^{-1}), between 30 min and 2 h were needed for the same simulation using Equation (66) for the liquid. Even though Nemat-Nasser is an explicit local solution method, it was only slightly faster than the local bounded NR method. However, benchmarks performed by Zhu *et al.* [3] found that the Nemat-Nasser method produced incorrect results for some viscoplastic laws, while the local bounded NR method was reliable in all cases. As found in Section 9, Abaqus implicit built-in integration (via CREEP subroutine) failed to converge, while explicit CREEP was very slow. There were no visible differences between any of the Abaqus stress results using the four different local integration algorithms that converged. CON2D had similar

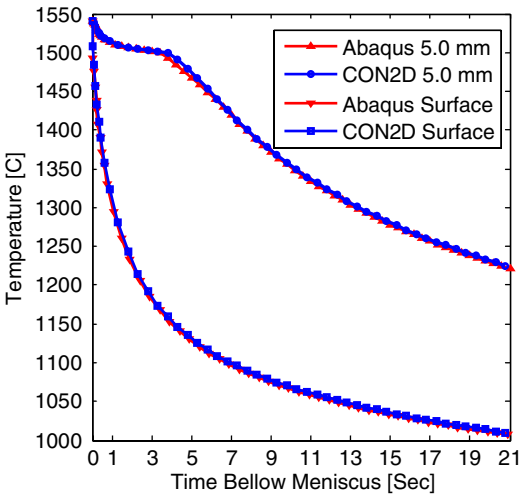

Figure 18. Temperature history for the surface material point and the material point 5 mm from the surface.

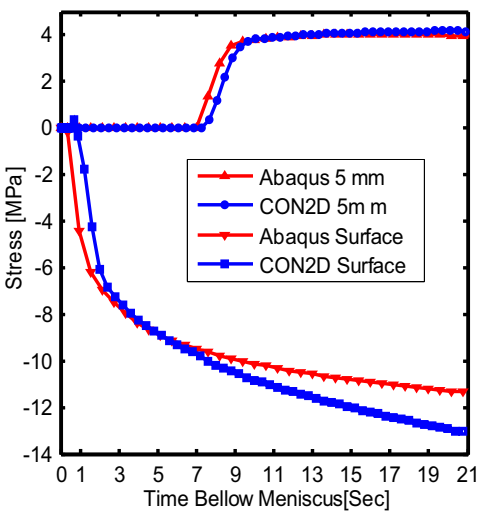

Figure 19. Lateral stress history for the surface material point and the material point 5 mm from the surface.

performance to Abaqus for the same local method, showing that the operator-splitting approach is reasonable, if the oscillations can be tolerated.

In conclusion, the implicit viscoplastic integration algorithm followed by the bounded NR scheme at the local level is the best, most robust method for solving solidification problems with highly nonlinear elastic-viscoplastic constutitive equations. Coding this method into

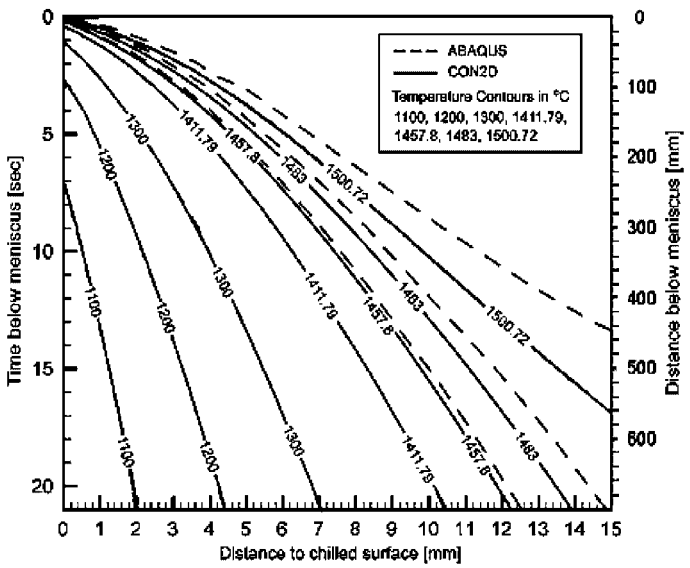

Figure 20. Temperature contours.

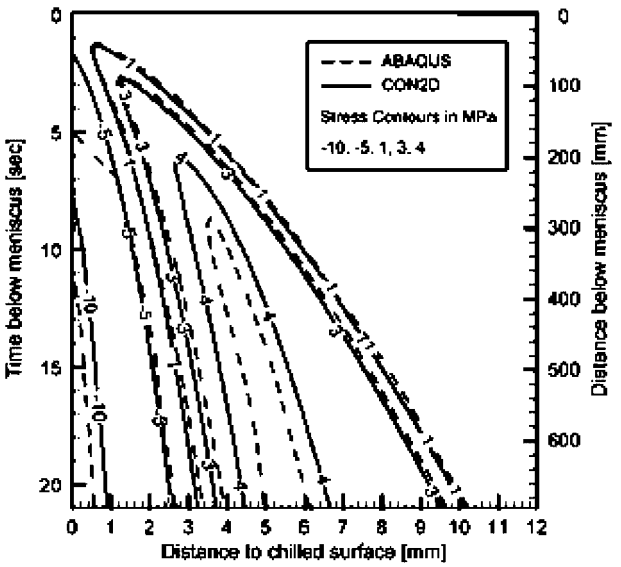

Figure 21. Stress contours.

a UMAT enables Abaqus to perform as well as the in-house CON2D code. Either full NR or operator-splitting are effective methods at the global level. The elastic-perfectly plastic algorithm (radial return) method is an efficient method to handle the liquid/mushy region.

Table II. CPU benchmark results.

Code	Global method for solving BVP	Local integration method	Treatment of liq./mushy zone	CPU time (min)
Abaqus	Full NR	Implicit followed by local bounded NR	Liquid function	55
Abaqus	Full NR	Implicit followed by Nemat–Nasser	Liquid function	53
Abaqus	Full NR	Implicit followed by local bounded NR	Radial return	5.6
Abaqus	Full NR	Implicit followed by full NR (CREEP)	Radial return or liquid function	Failed
Abaqus	Full NR	Explicit (CREEP)	Liquid function	185
CON2D	Operator splitting (initial strain)	Implicit followed by local bounded NR	Liquid function	6
CON2D	Operator splitting (initial strain)	Implicit followed by Nemat–Nasser	Liquid function	5.9

The rapid creep-type function for treating liquid (Equation (66)) has the advantage of accurately simulating liquid flow that is important for the quantitative prediction of hot tear cracks between dendrites at the solidification front [2, 52]. Using the UMAT, Abaqus is now ready to tackle large-scale finite-element simulations of solidification processes, including 3D analysis of continuous casting.

11. CONCLUSIONS AND FUTURE WORK

A class of highly nonlinear thermal-mechanical solidification problems is solved using several different local–global methods. The elastic-visco-plastic constitutive laws are integrated locally by four different integration methods. In addition to the local integration methods built into Abaqus, two new local integration schemes are coded into the Abaqus material user subroutine UMAT. At the global level, the full NR method built into the Abaqus finite element solution procedure is compared with the alternating implicit–explicit method of the in-house code CON2D. Results of both numerical codes are validated against a semi-analytical solution and both temperature and stress results match very well. The performance of Abaqus with the UMAT-coded methods is increased by ~ 20 times relative to the built-in method, and becomes comparable to CON2D.

This work should open the door for large-scale finite-element simulations of continuous casting and other solidification processes with highly nonlinear viscoplastic phenomena. In addition to temperature-dependent properties included in this work, more features will be implemented into future Abaqus solidification models. These will include ferrostatic pressure on the solidifying shell, mold distortion boundary condition data, contact algorithms with gap-dependent conductivity geometric nonlinearities, phase-dependent (delta-ferrite and austenite) constitutive laws, and segregation effects. With the powerful parallel solvers built into Abaqus on large shared memory platforms, this methodology will enable realistic simulations of continuous casting of steel and other processes in future work.

NOMENCLATURE

A	surface (m^2)
A_T	temp. prescribed surface (m^2)
A_q	flux prescribed surface (m^2)
A_h	convection prescribed surface (m^2)
A_u	displac. prescribed surface (m^2)
A_Φ	traction prescribed surface (m^2)
$[B]$	spatial derivative of $[N]$ (1/m)
b	gen plane strain const.
$\mathbf{b}$	volumetric force vector (N)
c_j	constant
c_s	sign of $\dot{\bar{\varepsilon}}_{ie}$
c_p	specific heat (J/kg K)
$[C]$	capacitance matrix (J/kg)
$\underline{\underline{\mathbf{D}}}$	fourth-order elasticity tens. (N/m^2)
E	elastic modulus (N/m^2)
$\mathbf{F}_q$	heat flow load vector (W)
F_z	ext. mech. force, gen. strain (N)
f	viscoplastic law function (1/s)
f_C	empirical constant ($MPa^{-f3}\,s^{-1}$)
f_1	empirical constant (MPa)
f_2	empirical constant
f_3	empirical constant
g	yield function
H	enthalpy (J/kg K)
Hf	latent heat (J/kg K)
HR	isotropic hardening (N/m^2)
$\underline{\underline{\mathbf{I}}}$	fourth-order identity tensor
$\underline{\mathbf{I}}$	second-order identity tensor
$\underline{\mathbf{J}}$	Jacobian (CTO) (N/m^2)
$\underline{\underline{k}}$	thermal conductivity (W/m K)
k_B	bulk modulus (N/m^2)
$[K]$	tangent matrix HT (W/K)
$[K]$	tangent matrix mech. (N/m)
$M_x M_y$	ext. mech. moments, gen str. (Nm)
$[N]$	element shape functions
$\mathbf{N}$	inelastic strain flow tensor (N/m^2)
$\mathbf{n}$	surface unit vector
$\mathbf{P}$	external force vector (N)
$\hat{q}$	prescribed heat flux (W/m^2)
Q	activation energy constant (K)
$\mathbf{R}$	residual force vector (N)
$\mathbf{S}$	internal force vector (N)
T	temperature (°C)

$\hat{T}$	prescribed BC temp. (°C)
T_∞	ambient temperature (°C)
T_{init}	initial temp. (°C)
T_{ref}	reference temperature (°C)
T_{sol}	solidus temp. (°C)
T_{liq}	liquidus temp. (°C)
TLE	thermal linear expansion
$\mathbf{u}$, $\mathbf{d}$	displacement vector (m)
V	volume (m^3)
$\mathbf{x}$	position vector (m)
α	coeff. of thermal expansion (1/°C)
β	constant
γ	constant
$\boldsymbol{\varepsilon}$	total strain tensor
$\Delta\hat{\boldsymbol{\varepsilon}}$	guess for tot. strain incr. tens.
$\dot{\boldsymbol{\varepsilon}}$	total strain rate tens. (1/s)
$\varepsilon_{\max}$	max. principal strain
$\varepsilon_{\min}$	min. principal strain
$\boldsymbol{\varepsilon}_{\text{el}}$	elastic strain tensor
$\dot{\boldsymbol{\varepsilon}}_{\text{el}}$	elastic strain rate tensor (1/s)
$\boldsymbol{\varepsilon}_{\text{ie}}$	inelastic strain tensor
$\dot{\boldsymbol{\varepsilon}}_{\text{ie}}$	inelastic strain rate tens. (1/s)
$\hat{\dot{\boldsymbol{\varepsilon}}}_{\text{ie}}$	guess for $\dot{\boldsymbol{\varepsilon}}_{\text{ie}}$ (1/s)
$\dot{\bar{\varepsilon}}_{\text{ie}}$	equivalent inelastic strain (1/s)
$\dot{\bar{\varepsilon}}^0_{\text{ie}}$	NN initial approx. of $\dot{\bar{\varepsilon}}_{\text{ie}}$ (1/s)
$\boldsymbol{\varepsilon}_{\text{th}}$	thermal strain tensor
$\dot{\boldsymbol{\varepsilon}}_{\text{th}}$	thermal strain rate tensor (1/s)
η	radial return factor
$\Delta\lambda$	plastic strain multiplier
μ	shear modulus (N/m^2)
μ_V	viscosity (Pa s)
$\boldsymbol{\sigma}$	stress tensor (N/m^2)
$\hat{\boldsymbol{\sigma}}$	guess for stress tensor (N/m^2)
$\boldsymbol{\sigma}'$	deviatoric stress tensor (N/m^2)
$\boldsymbol{\sigma}^*$	trial stress tensor (N/m^2)
$\bar{\sigma}$	equivalent stress (N/m^2)
$\bar{\sigma}^0$	NN initial approx. of $\bar{\sigma}$ (N/m^2)
$\Delta\bar{\sigma}^{\text{NR}}$	local NR $\bar{\sigma}$ correction (N/m^2)
$\Delta\bar{\sigma}^{\max}$	max. local BNR $\bar{\sigma}$ correction (N/m^2)
$\bar{\sigma}_{\text{lower}}$	lower bound for local BNR (N/m^2)
$\bar{\sigma}_{\text{upper}}$	upper bound for local BNR (N/m^2)
σ_{Y}	yield stress (N/m^2)
ρ	density (kg/m^3)
υ	Poisson's ratio
$\boldsymbol{\Phi}$	surface traction vector (N/m^2)

REFERENCES

1. Weiner JH, Boley BA. Elasto-plastic thermal stresses in a solidifying body. *Journal of the Mechanics and Physics of Solids* 1963; **11**:145–154.
2. Li C, Thomas BG. Thermo-mechanical finite-element model of shell behaviour in continuous casting of steel. *Metallurgical and Materials Transactions B* 2004; **35B**(6):1151–1172.
3. Zhu H. Coupled thermal-mechanical finite-element model with application to initial solidification. *Ph.D. Thesis*, University of Illinois, 1993.
4. Moitra A, Thomas BG, Zhu H. Application of thermo-mechanical model for steel behaviour in continuous slab casting. *Proceedings of the 76th Steelmaking Conference*, *ISS*, vol. 76, 1993.
5. Kristiansson JO. Thermal stresses in the early stage of solidification of steel. *Journal of Thermal Stresses* 1982; **5**:315–330.
6. Risso JM, Huespe AE, Cardona A. Thermal stress evaluation in the steel continuous casting process. *International Journal for Numerical Methods in Engineering*, in press.
7. Grill A, Brimacombe JK, Weinberg F. Mathematical analysis of stress in continuous casting of steel. *Ironmaking and Steelmaking* 1976; **3**:38–47.
8. Wimmer F, Thone H, Lindorfer B. Thermomechanically-coupled analysis of the steel solidification process in continuous casting mold. *Abaqus Users Conference*, 1996; 749–769.
9. Rammerstrofer FG, Jaquemar C, Fischer DF, Wiesinger H. Temperature fields, solidification progress and stress development in the strand during a continuous casting process of steel. *Numerical Methods in Thermal Problems*. Pineridge: Swansea, 1979; 712–722.
10. Kristiansson JO. Thermomechanical behavior of the solidifying shell within continuous casting billet molds—a numerical approach. *Journal of Thermal Stresses* 1984; **7**:209–226.
11. Lewis RW, Morgan K, Thomas HR, Seetharamu KN. *The Finite Element Method in Heat Transfer Analysis*. Wiley: New York, 1996.
12. Morgan K, Lewis RW, Williams JR. Thermal stress analysis of a novel continuous casting process. In *The Mathematics of Finite Elements and its Applications*, Whiteman JR (ed.) (V3 edn). Academic Press: New York, 1978.
13. Boehmer JR, Funk G, Jordan M, Fett FN. Strategies for coupled analysis of thermal strain history during continuous solidification processes. *Advances in Engineering Software* 1998; **29**(7–9):679–697.
14. Fachinotti VD, Cardona A. *A Fixed-mesh Eularian–Lagrangian Approach for Stress Analysis in Continuous Casting*. Instituto Argentina de Siderurgia: Argentina, 2002.
15. Farup I, Mo A. Two-phase modeling of mushy zone parameters associated with hot tearing. *Metallurgical and Materials Transactions* 2000; **31**:1461–1472.
16. Stangeland A, Mo A, Elskin ND, Hamdi, Development of thermal strain in the coherent mushy zone during solidification of aluminum alloys. *Metallurgical and Material Transactions* 1999; **30**:2903–2915.
17. Tan L, Zabaras N. A thermomechanical study of the effect of mold topography on the solidification of aluminum alloys. *Materials Science and Engineering*, in press.
18. Samanta D, Zabaras N. A coupled thermomechanical, thermal transport and segregation analysis of aluminum alloys solidifying on molds of uneven surfaces. *Materials Science and Engineering*, in press.
19. *Abaqus Theory Manual v6.4*. Abaqus Inc., 2004.
20. Lemmon EC. Multidimensional integral phase change approximations for finite element conduction codes. In *Numerical Methods in Heat Transfer*, Lewis R (ed.). Wiley: New York, NY, 1981; 201–213.
21. Dupont T, Fairweather G, Johnson J. Three-level Galerkin methods for parabolic equations. *SIAM Journal on Numerical Analysis* 1974; **11**:392–410.
22. Thomas BG, Brimacombe JK, Samarasekera IV. The formation of panel cracks in steel ingots, a state of the art review, part I—hot ductility of steel. *Transactions of the Iron and Steel Society* 1986; **7**:7–20.
23. Mase GE, Mase GT. *Continuum Mechanics for Engineers* (2nd edn). CRC Press: Boca Raton, FL, 1999.
24. Anand L. Constitutive equations for the rate dependent deformation of metals at elevated temperatures. *ASME Journal of Engineering Materials Technology* 1982; **104**:12–17.
25. Lush AM, Weber G, Anand L. An implicit time-integration procedure for a set of integral variable constitutive equations for isotropic elasto-viscoplasticity. *International Journal of Plasticity* 1989; **5**:521–549.
26. Mendelson A. *Plasticity*: *Theory and Applications*. Krieger: New York, 1983.
27. Lemaitre J, Chaboche JL. *Mechanics of Solid Materials*. Cambridge University Press: Cambridge, 2001.
28. *Abaqus Standard User Manuals v6.4*. Abaqus Inc., 2004.

29. Zienkiewicz OC, Taylor RL. *Finite Element Method*: *Solid and Fluid Mechanics Dynamics and Non-linearity*. McGraw-Hill: New York, 1991.
30. Stouffer DC, Dame LT. *Inelastic Deformation of Metals*: *Models*, *Mechanical Properties*, *Metallurgy*. Wiley: New York, 1995.
31. Simo JC, Taylor RL. Consistent tangent operators for rate independent elastoplasticity. *Computer Methods in Applied Mechanics and Engineering* 1985; **48**:101–118.
32. Crisfiled MA. *Nonlinear FEA of Solids and Structures*. Wiley: New York, 1991.
33. Glowinski R, Tallee PL. *Augmented Lagrangian and Operator-splitting Methods in Non-linear Mechanics*. SIAM: Philadelphia, PA, 1989.
34. Zienkiewicz OC, Cormeau IC. Visco-plasticity-plasticity and creep in elastic solids—a unified numerical solution approach. *International Journal for Numerical Methods in Engineering* 1974; **8**:821–845.
35. Guidelines for writing user subroutine CREEP. Attachment to answer #805 from abaqus online support system. http://www.abaqus.com (May 2005).
36. Zabaras N, Arif ABFM. A family of integration algorithms for constitutive equations in finite difference deformations elasto-viscoplasticity. *International Journal for Numerical Methods in Engineering* 1992; **33**: 59–84.
37. Continuous Casting Consortium Website. http://ccc.me.uiuc.edu (30 October 2005).
38. Nemat-Nasser S, Li YF. A new explicit algorithm for finite-deformation elastoplasticity and elastovisco-plasticity: performance evaluation. *Computers and Structures* 1992; **44**(5):937–963.
39. Nemat-Nasser S, Chung DT. An explicit constitutive algorithm for large-strain, large-strain-rate elastic-viscoplasticity. *Computer Methods in Applied Mechanics and Engineering* 1992; **95**:205–219.
40. *ANSYS 5.3*. Swanson Analysis Systems, Inc.: Houston, PA, 2005.
41. Belytschko T, Liu WK, Moran B. *Nonlinear FE for Continua and Structures*. Wiley: New York, 2000.
42. Rappaz M, Drezet J, Gremaud M. A new hot-tearing criterion. *Metallurgical and Materials Transactions A* 1999; **30A**:449–455.
43. Kozlowski PF, Thomas BG, Azzi JA, Wang H. Simple constitutive equations for steel at high temperature. *Metallurgical Transactions* 1992; **23A**:903–918.
44. Wray PJ. Plastic deformation of delta-ferritic iron at intermediate strain rates. *Metallurgical and Materials Transactions* 1976; **7A**:1621–1627.
45. Suzuki T, Tacke KH, Wunnenberg K, Schwerdtfeger K. Creep properties of steel at continuous casting temperatures. *Ironmaking and Steelmaking* 1988; **15**(2):90–100.
46. Pehlke RD, Jeyarajan A, Wada H. Summary of thermal properties for casting alloys and mould materials. *Report No. NSF/MEA-82028*, Department of Materials and Metallurgical Engineering, University of Michigan, 1982, PB83 211003.
47. Harste K. Investigation of the shrinkage and the origin of mechanical tension during the solidification and successive colling of cylindrical bars of Fe-C alloys. *Ph.D. Thesis*, Technical University of Clausthal, 1989.
48. Huang X, Thomas BG, Najjar FM. Modeling superheat removal during continuous casting of steel slabs. *Metallurgical Transactions B* 1992; **23B**:339–356.
49. Harste K, Jablonka A, Schwerdtfeger K. Shrinkage and formation of mechanical stresses during solidification of round steel strands. *4th International Conference Continuous Casting*, Brussels, Belgium, vol. 2. Verlag Stahleisen, P.O. Box 8229, D-4000, Dusseldorf 1, FRG, 2, 1988; 633–644 (preprints).
50. Jimbo I, Cramb AAW. The density of liquid iron–carbon alloys. *Metallurgical Transactions B* (U.S.A.) 1993; **24B**(1):5–10.
51. Mizukami H, Murakami K, Miyashita Y. Tetsu-to-Hagane. Elastic modulus of steels at high temperature. *Journal of the Iron and Steel Institute of Japan* 1977; **63**(146):S-652.
52. Li C, Thomas BG. Maximum casting speed for continuous cast steel billets based on sub-mold bulging computation. *Steelmaking Conference Proceedings 2002*, *ISS*, Warrendale, PA, Nashville, TN, 10–13 March 2002; 109–130 .

